nature physics

Article

https://doi.org/10.1038/s41567-024-02493-1

Single-component superconductivity in UTe_2 at ambient pressure

Received: 19 July 2023

Accepted: 28 March 2024

Published online: 09 May 2024

Check for updates

Florian Theuss[1], Avi Shragai[1], Gaël Grissonnanche[1,2,3], Ian M. Hayes[4], Shanta R. Saha[4], Yun Suk Eo[4], Alonso Suarez[4], Tatsuya Shishidou[5], Nicholas P. Butch[4,6], Johnpierre Paglione[4,7] & B. J. Ramshaw[1,7]

The microscopic mechanism of Cooper pairing in a superconductor leaves its fingerprint on the symmetry of the order parameter. UTe_2 has previously been inferred to have a multi-component order parameter, in part due to the apparent presence of a two-step superconducting transition in some samples. However, recent experimental observations in newer-generation samples have raised questions about this interpretation, pointing to the need for a direct probe of the order parameter symmetry. Here we use pulse-echo ultrasound to measure the elastic moduli of UTe_2 in samples that exhibit both one and two superconducting transitions. We demonstrate the absence of thermodynamic discontinuities in the shear elastic moduli of both single- and double-transition samples, providing direct evidence that UTe_2 has a single-component superconducting order parameter. We further show that superconductivity is highly sensitive to compression strain along the *a* and *c* axes but insensitive to strain along the *b* axis. This leads us to suggest a single-component, odd-parity order parameter—specifically the B_{2u} order parameter—as most compatible with our data.

Definitive determination of the superconducting pairing symmetry has been accomplished for only a handful of materials, among them the *s*-wave Bardeen–Cooper–Schrieffer superconductors and the *d*-wave cuprates[1]. In some superconductors, such as Sr_2RuO_4, debate over the pairing symmetry has persisted for decades despite ultra-pure samples and an arsenal of experimental techniques[2–4]. This is more than an issue of taxonomy: the pairing symmetry places strong constraints on the microscopic mechanism of Cooper pairing, and some pairing symmetries can lead to topological superconducting states[5].

The question of pairing symmetry is nowhere more relevant than in UTe_2, where in addition to power laws in thermodynamic quantities[6–9], the most striking evidence for unconventional superconductivity is an extremely high upper critical field H_{c2} compared with the relatively low critical temperature[7,10]. Remarkably, for some field orientations, the superconductivity re-emerges from a resistive state above approximately 40 T and persists up to at least 60 T (ref. 11). This high H_{c2} constrains the spin component of the Cooper pair to be spin-triplet, which in turn constrains the orbital component of the Cooper pair to be odd under inversion (that is odd parity, such as a *p*- or *f*-wave state). However, there are many possible odd-parity order parameters and which one—or which pair, if UTe_2 is a two-component superconductor as suggested[12]—manifests in UTe_2 is unknown.

The primary question we address here is regarding the degeneracy of the orbital part of the superconducting order parameter. In addition to even (*s*- or *d*-wave) and odd (*p*- and *f*-wave) designations, order parameters can have multiple components: both conventional *s*-wave and high-T_c $d_{x^2-y^2}$-wave order parameters are described by a single complex number, whereas the topological $p_x + ip_y$ state has two components, namely p_x and p_y. Evidence for a two-component order parameter in UTe_2 stems from the presence of two distinct superconducting

[1]Laboratory of Atomic and Solid State Physics, Cornell University, Ithaca, NY, USA. [2]Kavli Institute at Cornell for Nanoscale Science, Ithaca, NY, USA. [3]Laboratoire des Solides Irradiés, CEA/DRF/IRAMIS, CNRS, École Polytechnique, Institut Polytechnique de Paris, Palaiseau, France. [4]Maryland Quantum Materials Center, Department of Physics, University of Maryland, College Park, MD, USA. [5]Department of Physics, University of Wisconsin-Milwaukee, Milwaukee, WI, USA. [6]NIST Center for Neutron Research, National Institute of Standards and Technology, Gaithersburg, MD, USA. [7]Canadian Institute for Advanced Research, Toronto, Ontario, Canada. e-mail: bradramshaw@cornell.edu

https://doi.org/10.1038/s41567-024-02493-1

Table 1 | Proposed order parameters for UTe_2

Dimensionality	Representation	Shear discontinuity?	Reference (E, experiment; T, theory)
One component	A_u	No	E: NMR[30]
			E: scanning SQUID[31]
	B_{2u}	No	E: ultrasound (this work)
	B_{3u}	No	T: DFT[32]
			E: NMR[33,34]
			E: scanning SQUID[31]
		No	E: specific heat[16,17]
			E: uniaxial stress[26]
Two component	$\{B_{1u}, A_u\}$	c_{66}	E: microwave surface impedance[15]
			E: specific heat, Kerr effect[12]
	$\{B_{3u}, A_u\}$	c_{44}	E: penetration depth[8]
			E: NMR[35]
	$\{B_{1u}, B_{2u}\}$	c_{44}	T: ^{3}He A-phase-like pairing[36,37]
			E: specific heat[9]
	$\{B_{1u}, B_{3u}\}$	c_{55}	T: phenomenology + DFT[38]
			T: DFT[39]
	$\{B_{2u}, B_{3u}\}$	c_{66}	T: DFT[22,23]
			E: specific heat, Kerr effect[12,13]
			T: emergent D_{4h} symmetry[24]
		Yes	E: STM[14]
			T: pair-Kondo effect[40]
			T: MFT of Kondo lattice[41]

Proposed odd-parity order parameters for UTe_2, sorted by the number of components (dimensionality), their irreducible representation and whether the proposed order parameter is based on an experimental observation or a theoretical proposal. Scenarios listed without a specific representation are compatible with any type of one- or two-component order parameter. On the basis of symmetry alone, our work strongly constrains the order parameter to be of the one-component type. Using more quantitative arguments, we suggest a B_{2u} order parameter. NMR, nuclear magnetic resonance; SQUID, superconducting quantum interference device; DFT, density functional theory.

transitions in some samples, as well as from the onset of time-reversal symmetry breaking at T_c (refs. 12,13). Combined with evidence for spin-triplet pairing, these observations have led to several proposed exotic, multi-component order parameters for UTe_2 (Table 1). These multi-component states can have a topological structure that could explain other experimental observations, such as the chiral surface states seen in scanning tunnelling microscopy (STM)[14] or the anomalous normal component of the conductivity observed in microwave impedance measurements[15].

Claims of a multi-component order parameter are not without controversy, however. As the purity of the samples has increased, T_c has shifted to higher values and the second transition has disappeared at ambient pressure[16]. Previous work has suggested that two transitions arise due to inhomogeneity[17], but the application of hydrostatic pressure splits single-T_c samples into two-T_c samples[18,19], suggesting that two superconducting order parameters are, at the very least, nearly degenerate with one another.

The natural way to distinguish between single-component and two-component order parameters is to apply strain. Single-component superconductors have a single degree of freedom—the superfluid density—that couples to compression strains, producing a discontinuity in the compressional elastic moduli at T_c (Fig. 1). Single-component superconductors, however, have no such discontinuity in their shear moduli because shear strains preserve volume and thus do not couple to superfluid density. Multi-component superconductors, on the other hand, have additional degrees of freedom: the relative orientation of the two order parameters, as well as their relative phase difference. These additional degrees of freedom couple to shear strains, producing discontinuities in the shear moduli at T_c. By identifying which elastic moduli have discontinuities at T_c, one can determine whether a superconductor is multi-component without any microscopic knowledge of the Fermi surface or the pairing mechanism.

Results

We use a traditional phase-comparison pulse-echo ultrasound technique to measure the temperature dependence of six elastic moduli in three different samples of UTe_2 over a temperature range from approximately 1.3 to 1.9 K. In particular, we measure all three compressional (that is, c_{11}, c_{22} and c_{33}) and shear (that is, c_{44}, c_{55} and c_{66}) moduli in one sample with two superconducting transitions (S3: $T_{c,1} \approx 1.64$ K, $T_{c,2} \approx 1.60$ K) and in two samples with a single T_c (S1: $T_c \approx 1.63$ K and S2: $T_c \approx 1.70$ K). Ultrasound data in the normal state of UTe_2 have been reported by Ushida et al.[20]. Here, we focus on the superconducting transition. Details of the sample growth and preparation, as well as the experiment, are given in Methods.

Figure 2 shows the relative changes in four elastic moduli across T_c for the single-transition samples S1 and S2. We observe a single, sharp (approximately 85 mK wide) discontinuity in the c_{33} compressional modulus, as expected for all superconducting transitions. We observe no discontinuities in any of the shear elastic moduli to within our experimental resolution (a few parts in 10^7; see Supplementary Figs. 5 and 6 for details).

Figure 3 shows the relative changes in the elastic moduli for sample S3 with a double superconducting transition (the single-T_c data are reproduced here for comparison). We observe two distinct discontinuities in c_{33} separated by approximately 40 mK. Subsequent specific heat measurements on the same sample show a similar double peak feature identified in other double-T_c samples[12] (specific heat data are shown in Supplementary Fig. 7). Notably, we find the sum of the discontinuities in the double-T_c sample to be of a similar size as the discontinuity in the single-T_c sample. Additionally, the behaviour of the shear elastic moduli is nearly identical to that of the single-T_c samples, again with no discontinuities at T_c.

We also measure the two other compressional moduli—c_{11} and c_{22}—and show them along with c_{33} in Fig. 4. c_{11} has a discontinuity of approximately 20 parts per million—roughly a factor of 2 smaller than the discontinuity in c_{33}. In contrast, c_{22} has a discontinuity of at most 1 part per million—significantly smaller than the other two compressional moduli. Discontinuities in all three compressional moduli are allowed by symmetry for any superconducting order parameter (see ref. 2 and 'Landau free energy calculations' section in Supplementary Information).

We first analyse the data using only the presence or absence of discontinuities in the elastic moduli. This analysis is based on symmetry arguments alone and is independent of the size of the discontinuities. We then perform a quantitative analysis of the discontinuities using Ehrenfest relations. Finally, we combine all of our observations to speculate on which particular superconducting order parameter is most consistent with our data.

https://doi.org/10.1038/s41567-024-02493-1

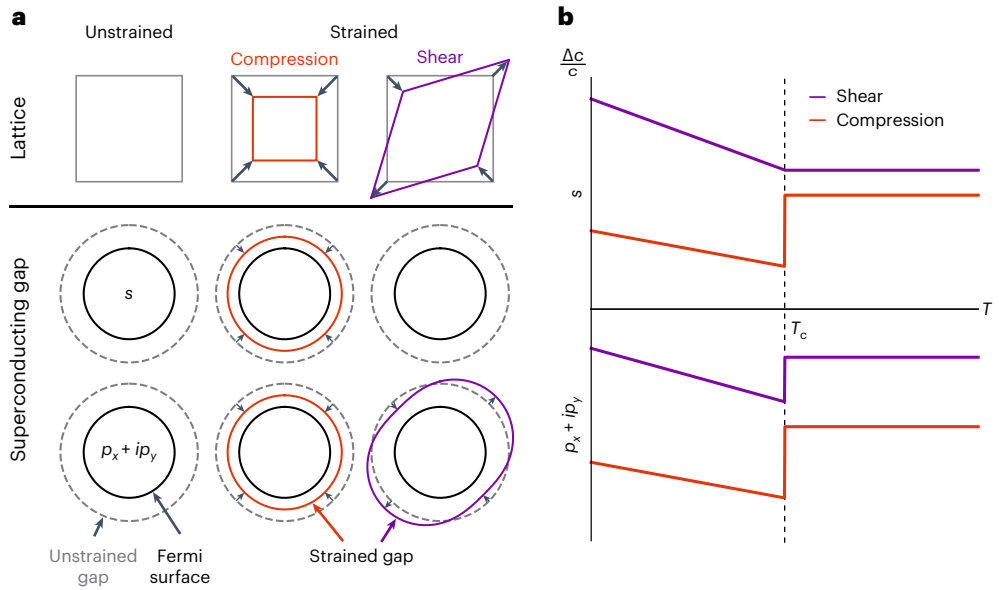

Fig. 1 | The influence of strain on one- and two-component superconductors. **a**, An illustration of how two representative order parameters—single-component *s*-wave and two-component $p_x + ip_y$—respond to both compression and shear strain. Both gaps respond under compression (whether increasing or decreasing in magnitude depends on microscopic details). Only the two-component gap, however, couples to shear strain—here we illustrate the phase mode (see ref. 2 for more details). **b**, The expected changes in elastic moduli across T_c for one- and two-component order parameters. All superconductors have a discontinuity in their compressional moduli across T_c, but only two-component superconductors have discontinuities in their shear moduli.

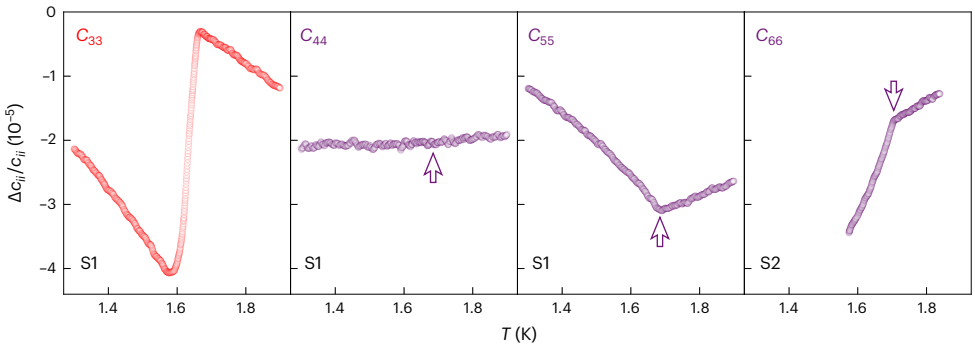

Fig. 2 | Relative change in elastic moduli through T_c for single-T_c UTe_2. The compressional elastic modulus c_{33} shows a sharp discontinuity—as expected for all superconductors—of approximately 40 parts per million at T_c. In contrast, the shear elastic moduli c_{44}, c_{55} and c_{66} show only changes in slope at T_c, consistent with a single-component superconducting order parameter. Arrows mark the superconducting transition for all shear moduli. $\Delta c_{ii}/c_{ii}$ is defined as $(c_{ii}(T) - c_{ii}(T_0))/c_{ii}(T_0)$, where T_0 is the highest temperature shown.

Symmetry of the superconducting order parameter

The presence or absence of a discontinuity in each elastic modulus constrains the symmetry of the superconducting order parameter. Roughly speaking, only strains that couple linearly to a degree of freedom associated with the superconducting order parameter show discontinuities at T_c. We illustrate this with a couple of examples; a more rigorous derivation is given in 'Landau free energy calculations' in Supplementary Information.

Discontinuities in elastic moduli arise when there is coupling between strain and superconductivity that is linear in strain and quadratic in the order parameter. For a single-component superconducting order parameter, this only occurs for compression strains[21]. A single-component order parameter can be written as $\eta = \eta_0 e^{i\phi}$, where η_0 is the magnitude of the gap (which may depend on momentum) and ϕ is the superconducting phase. The lowest-order coupling to a strain ϵ_{ij} is $\epsilon_{ij}\eta^\star\eta = \epsilon_{ij}\eta_0^2$, where the asterisk denotes complex conjugation. This coupling is allowed only if ϵ_{ij} preserves the symmetry of the lattice; that is, it is only allowed for compression strains and not for shear strains (which break the lattice symmetry). Since η_0^2 is proportional to the superfluid density, the physical interpretation of the resulting discontinuity at T_c is that compression strain couples to the superfluid density, which turns on at T_c and provides a new degree of freedom that softens the lattice.

In contrast to single-component order parameters, multi-component order parameters can have discontinuities in shear elastic moduli. This is because there are more degrees of freedom associated with a multi-component order parameter than with a single-component order parameter. Writing a two-component order parameter as $\vec{\eta} = \{\eta_{0,i}e^{i\phi_i}, \eta_{0,j}e^{i\phi_j}\}$, there are now several possible couplings at lowest order. Taking the well-known $p_x + ip_y$ state in tetragonal crystals as an example, one possible coupling is $\epsilon_{xy}\eta_{0,p_x}\eta_{0,p_y}\cos\left(\phi_{p_x} - \phi_{p_y}\right)$. This is the so-called phase mode of the order parameter, as it couples ϵ_{xy} shear strain to the relative phase of the two components (Fig. 1). This produces a discontinuity in the associated elastic modulus c_{66}. The relative phase is a new degree of freedom that is only present in a multi-component order parameter, as strain

https://doi.org/10.1038/s41567-024-02493-1

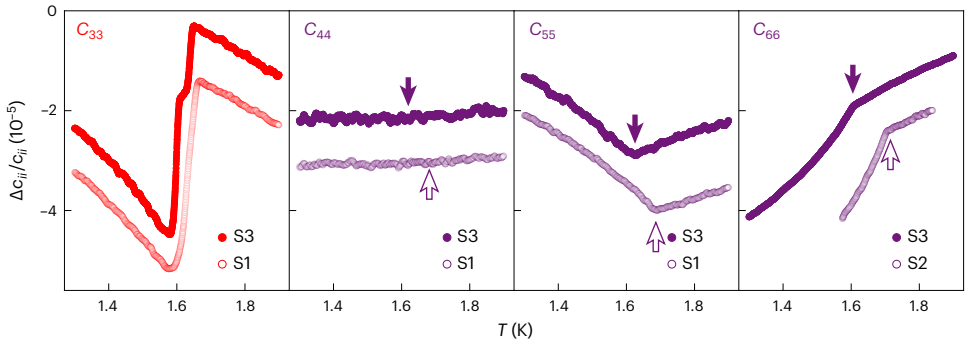

Fig. 3 | Relative change in elastic moduli through T_c for double-T_c UTe_2. The compressional elastic modulus c_{33} shows two distinct discontinuities at T_c, consistent with the two peaks we find in the specific heat of the same sample. The shear moduli, on the other hand, show no discontinuities and behave nearly identically to the shear moduli of the single-T_c sample. Single-(double-)transition samples are shown with empty (filled) symbols. Empty (filled) arrows mark the superconducting transition for all shear moduli for single-(double-)transition samples. $\Delta c_{ii}/c_{ii}$ is defined as in Fig. 2, and curves have been offset vertically for clarity.

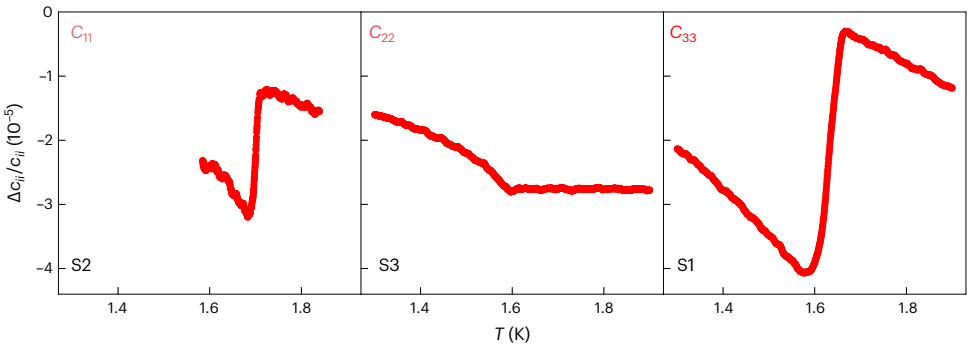

Fig. 4 | Relative change in compressional elastic moduli through T_c. The compressional elastic moduli as functions of temperature through T_c. c_{33} and c_{11} were measured on a single-T_c sample, and c_{22} was measured on the double-T_c sample. Both c_{11} and c_{33} show clearly resolvable discontinuities at T_c, whereas c_{22} shows a barely resolvable discontinuity. $\Delta c_{ii}/c_{ii}$ is defined as in Fig. 2.

cannot couple to the absolute phase of a single-component order parameter (such a term would break gauge symmetry). Similar expressions exist for orthorhombic crystals (see 'Landau free energy calculations' section in Supplementary Information for details), but the main conclusion is independent of the crystal structure: shear elastic moduli only exhibit discontinuities at T_c for multi-component superconducting order parameters.

The absence of a discontinuity in any shear elastic modulus in the single-transition samples (S1 and S2) rules out essentially all two-component order parameters in UTe_2. While there are no natural two-component order parameters in UTe_2 because the crystal structure is orthorhombic, many nearly or accidentally degenerate order parameters have been proposed to explain the presence of the two nearly degenerate T_c's, time reversal symmetry breaking and chiral surface states (Table 1). One proposal is the onset of first a B_{2u} state followed by a B_{3u} state at the second, lower T_c (refs. 12,13,22–24). This proposal predicts the usual discontinuities in compressional moduli at the first (higher) T_c, followed by a discontinuity in the compressional moduli and the c_{66} shear modulus at the lower T_c. In fact, the product of any two odd-parity (that is p- or f-wave) states or any two even-parity (that is s- or d-wave) states in D_{2h} predicts a discontinuity in either c_{44}, c_{55} or c_{66}, none of which we observe. This strongly constrains the superconducting order parameter of UTe_2 to be of the single-component type. Finally, we note that our data are fully consistent with any single-component order parameter, including even-parity states such as s-wave and d-wave.

The similar absence of discontinuities in the shear elastic moduli of the two-transition sample (S3) rules out the multi-component explanation for the second superconducting transition. We find that the single discontinuity in c_{33} in single-T_c samples is approximately the same size as the sum of the two discontinuities found in double-T_c samples. This suggests that, below the second transition, all electrons in UTe_2 are in the same thermodynamic state, rather than double-T_c samples having two separate superconducting mechanisms. This suggests a common origin for the two superconducting transitions, perhaps split by local strains[17] or magnetic impurities[25]. Why this usually manifests as only two sharp T_c's (as we also observe in our data), rather than as multiple T_c's or as a broad transition, remains an open question. It also leaves unresolved the issue of why even single-T_c samples become double-T_c samples under hydrostatic pressure, leaving open the possibility of a multi-component order parameter under pressure.

Coupling of compression strains to superconductivity

The smallness of the discontinuity in c_{22} compared with the other two compressional moduli indicates that the superconductivity in UTe_2 is insensitive to strain along the b axis (ϵ_{yy}). This observation is made quantitative through Ehrenfest relations, which relate discontinuities in the elastic moduli, δc_{ij}, to the discontinuity in the specific heat, ΔC. The Ehrenfest relations are

$$\delta c_{ij} = -\frac{\Delta C}{T}\left(\frac{\mathrm{d}T_c}{\mathrm{d}\epsilon_{ij}}\right)^2, \quad (1)$$

https://doi.org/10.1038/s41567-024-02493-1

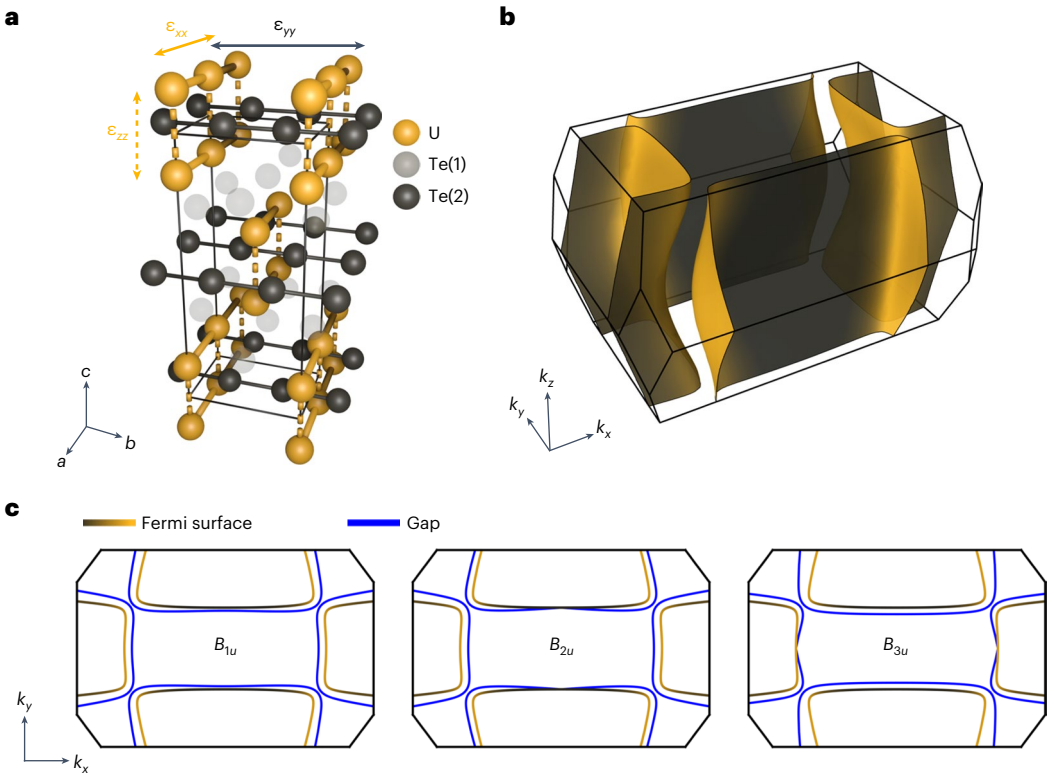

Fig. 5 | Influence of compression strains on the crystal structure and Fermi surface of UTe_2. a, The crystal structure of UTe_2. Highlighted are tellurium chains along the *b* axis and chains that run along the *a* axis consisting of *c*-axis-oriented uranium dimers. **b**, The geometry of the Fermi surface, modelled after quantum oscillation measurements, which is dominated by the chains shown in **a**[27]. The Fermi surface is coloured according to its uranium (yellow) and tellurium (grey) content. **c**, The superconducting gaps (blue lines) for three possible odd-parity order parameters at $k_z = 0$.

where $\frac{dT_c}{d\epsilon_{ij}}$ is the derivative taken at zero applied stress. Using the specific heat measured on sample S3 (Supplementary Figs. 7 and 8) and the data shown in Fig. 4, we calculate $\frac{dT_c}{d\epsilon_{xx}} = 0.23 \pm 0.02$ K per % strain, $\frac{dT_c}{d\epsilon_{yy}} = 0.07 \pm 0.02$ K per % strain and $\frac{dT_c}{d\epsilon_{zz}} = 0.34 \pm 0.02$ K per % strain. These values are roughly consistent with those measured in uniaxial strain experiments[26] (see Supplementary Table 2 for a quantitative comparison).

These Ehrenfest relations indicate that the superconductivity of UTe_2 is substantially more sensitive to strains along the *a* and *c* axes than it is to strain along the *b* axis. This observation is perhaps surprising given the relatively quasi-two-dimensional nature of the Fermi surface measured by quantum oscillations in UTe_2 (refs. 27,28). This Fermi surface consists of two sets of quasi-one-dimensional sheets running along the *a* and *b* axes that hybridize to form one electron and one hole pocket (Fig. 5). Thus, if any direction is to be weakly coupled to superconductivity, one might expect it to be the *c* axis. This argument is unchanged by the possible existence of an additional small pocket of Fermi surface reported by Broyles et al.[29], as it is roughly isotropic and thus does not single out any particular direction.

Looking at the crystal structure in Fig. 5, however, it is clear that the *a* and *b* axes are very different: chains of *c*-axis-coupled uranium dimers run along the *a* axis, whereas chains of tellurium run along the *b* axis (the other tellurium site, Te(1), participates much less in the Fermi surface than the Te(2) chains; Supplementary Figs. 9 and 10). Thus, ϵ_{xx} and ϵ_{zz} modulate the inter- and intra-dimer coupling of the uranium dimers, respectively, whereas ϵ_{yy} only modulates the weak inter-chain coupling of the uranium chains. ϵ_{yy} does, however, modulate the spacing between tellurium atoms in the tellurium chains that run along the *b* axis. Our observation of the relative insensitivity of T_c to ϵ_{yy} therefore suggests that the superconducting pairing is more sensitive to the uranium–uranium distances than to the tellurium–tellurium distances.

Proposed single-component superconducting order parameter

Thermal transport[6], specific heat[7,9] and penetration depth[8] all suggest the presence of point nodes in the superconducting gap of UTe_2. B_{1u}, B_{2u} and B_{3u} order parameters all have point nodes in their superconducting gaps, but these nodes lie along different directions in momentum space and thus intersect different portions of the Fermi surface (or may not intersect the Fermi surface at all if it is quasi-2D).

We use our observation of relatively weak coupling between ϵ_{yy} and T_c to motivate a particular orientation of the point nodes in UTe_2 and to suggest one particular single-component order parameter. Figure 5 shows a tight binding model of the Fermi surface of UTe_2 as determined by quantum oscillations, colour-coded by the relative uranium 6*d* and tellurium 5*p* content (both bands have substantial uranium 5*f* character that contributes to their heavy masses but not to their geometry). Our results suggest that the superconducting gap is either weak or absent on the tellurium-dominant electron Fermi surface. Only the B_{2u} order parameter has nodes that lie along the k_y direction, producing a node in the gap on the tellurium-dominant surface and a gap maximum on the uranium-dominant surface. We note that a reported small pocket with a light mass does not qualitatively affect this argument[29], as it is largely isotropic in shape and thus will not respond differently to ϵ_{xx} and ϵ_{yy} strain.

Discussion

Our discovery of a single-component order parameter places strong constraints on possible explanations for other experimental observations. First, a single-component order parameter cannot break

time reversal symmetry. This suggests that the interpretation of time reversal symmetry breaking at T_c as seen by polar Kerr effect measurements[12,13], along with the chiral surface states seen in STM[14] and microwave surface impedance measurements[15], needs to be revisited.

The search for multi-component superconductors continues: they are of both fundamental and practical interest, since a multi-component order parameter is a straightforward route to topological superconductivity. We find that, while UTe_2 may have an odd-parity, spin-triplet order parameter, it seems that the most likely order parameter to condense at T_c is of the single-component B_{2u} representation: either p_y- or f_{yz^2}-wave superconductivity. Definitive determination of the orientation of the nodes in the superconducting gap would confirm this scenario.

Online content

Any methods, additional references, Nature Portfolio reporting summaries, source data, extended data, supplementary information, acknowledgements, peer review information; details of author contributions and competing interests; and statements of data and code availability are available at https://doi.org/10.1038/s41567-024-02493-1.

References

1. Tsuei, C. C. & Kirtley, J. R. Pairing symmetry in cuprate superconductors. *Rev. Mod. Phys.* **72**, 969–1016 (2000).
2. Ghosh, S. et al. Thermodynamic evidence for a two-component superconducting order parameter in Sr_2RuO_4. *Nat. Phys.* **17**, 199–204 (2021).
3. Rice, T. M. & Sigrist, M. Sr_2RuO_4: an electronic analogue of ^{3}He? *J. Phys. Condensed Matter* **7**, L643–L648 (1995).
4. Mackenzie, A. P., Scaffidi, T., Hicks, C. W. & Maeno, Y. Even odder after twenty-three years: the superconducting order parameter puzzle of Sr_2RuO_4. *npj Quantum Mater.* **2**, 40 (2017).
5. Sato, M. & Ando, Y. Topological superconductors: a review. *Rep. Prog. Phys.* **80**, 076501 (2017).
6. Metz, T. et al. Point-node gap structure of the spin-triplet superconductor UTe_2. *Phys. Rev. B* **100**, 220504 (2019).
7. Ran, S. et al. Nearly ferromagnetic spin-triplet superconductivity. *Science* **365**, 684–687 (2019).
8. Ishihara, K. et al. Chiral superconductivity in UTe_2 probed by anisotropic low-energy excitations. *Nat. Commun.* **14**, 2966 (2023).
9. Kittaka, S. et al. Orientation of point nodes and nonunitary triplet pairing tuned by the easy-axis magnetization in UTe_2. *Phys. Rev. Res.* **2**, 032014 (2020).
10. Aoki, D. et al. Unconventional superconductivity in heavy fermion UTe_2. *J. Phys. Soc. Jpn* **88**, 043702 (2019).
11. Ran, S. et al. Extreme magnetic field-boosted superconductivity. *Nat. Phys.* **15**, 1250–1254 (2019).
12. Hayes, I. M. et al. Multicomponent superconducting order parameter in UTe_2. *Science* **373**, 797–801 (2021).
13. Wei, D. S. et al. Interplay between magnetism and superconductivity in UTe_2. *Phys. Rev. B* **105**, 024521 (2022).
14. Jiao, L. et al. Chiral superconductivity in heavy-fermion metal UTe_2. *Nature* **579**, 523–527 (2020).
15. Bae, S. et al. Anomalous normal fluid response in a chiral superconductor UTe_2. *Nat. Commun.* **12**, 2644 (2021).
16. Rosa, PriscilaF. S. et al. Single thermodynamic transition at 2 K in superconducting UTe_2 single crystals. *Commun. Mater.* **3**, 1–6 (2022).
17. Thomas, S. M. et al. Spatially inhomogeneous superconductivity in UTe_2. *Phys. Rev. B* **104**, 224501 (2021).
18. Aoki, D. et al. Multiple superconducting phases and unusual enhancement of the upper critical field in UTe_2. *J. Phys. Soc. Jpn* **89**, 053705 (2020).
19. Braithwaite, D. et al. Multiple superconducting phases in a nearly ferromagnetic system. *Commun. Phys.* **2**, 147 (2019).
20. Ushida, K. et al. Lattice instability of UTe_2 studied by ultrasonic measurements. *JPS Conf. Proc.* **38**, 011021 (2023).
21. Rehwald, W. The study of structural phase transitions by means of ultrasonic experiments. *Adv. Phys.* **22**, 721–755 (1973).
22. Shishidou, T., Suh, HanGyeol, Brydon, P. M. R., Weinert, M. & Agterberg, D. F. Topological band and superconductivity in UTe_2. *Phys. Rev. B* **103**, 104504 (2021).
23. Choi, H. C., Lee, S. H., & Yang, B.-J. Correlated normal state fermiology and topological superconductivity in UTe_2. Preprint at https://arxiv.org/abs/2206.04876 (2023).
24. Shaffer, D. & Chichinadze, D. V. Chiral superconductivity in UTe_2 via emergent C_4 symmetry and spin-orbit coupling. *Phys. Rev. B* **106**, 014502 (2022).
25. Sundar, S. et al. Ubiquitous spin freezing in the superconducting state of UTe_2. *Commun. Phys.* **6**, 24–34 (2023).
26. Girod, Clément et al. Thermodynamic and electrical transport properties of UTe_2 under uniaxial stress. *Phys. Rev. B* **106**, L121101 (2022).
27. Eaton, A. G. et al. Quasi-2D Fermi surface in the anomalous superconductor UTe_2. *Nat. Commun.* **15**, 223 (2024).
28. Aoki, D. et al. First observation of the de Haas–van Alphen effect and Fermi surfaces in the unconventional superconductor UTe_2. *J. Phys. Soc. Jpn* **91**, 083704 (2022).
29. Broyles, C. et al. Revealing a 3D Fermi surface pocket and electron-hole tunneling in UTe_2 with quantum oscillations. *Phys. Rev. Lett.* **131**, 036501 (2023).
30. Matsumura, H. et al. Large reduction in the *a*-axis Knight shift on UTe_2 with T_c=2.1 K. *J. Phys. Soc. Jpn* **92**, 063701 (2023).
31. Iguchi, Y. et al. Microscopic imaging homogeneous and single phase superfluid density in UTe_2. *Phys. Rev. Lett.* **130**, 196003 (2023).
32. Xu, Y., Sheng, Y. & Yang, Yi-feng Quasi-two-dimensional Fermi surfaces and unitary spin-triplet pairing in the heavy fermion superconductor UTe_2. *Phys. Rev. Lett.* **123**, 217002 (2019).
33. Fujibayashi, H. et al. Superconducting order parameter in UTe_2 determined by Knight shift measurement. *J. Phys. Soc. Jpn* **91**, 043705 (2022).
34. Nakamine, G. et al. Anisotropic response of spin susceptibility in the superconducting state of UTe_2 probed with ^{125}Te-NMR measurement. *Phys. Rev. B* **103**, L100503 (2021).
35. Nakamine, G. et al. Inhomogeneous superconducting state probed by ^{125}Te NMR on UTe_2. *J. Phys. Soc. Jpn* **90**, 064709 (2021).
36. Machida, K. Theory of spin-polarized superconductors—an analogue of superfluid ^{3}He A-phase. *J. Phys. Soc. Jpn* **89**, 033702 (2020).
37. Machida, K. Nonunitary triplet superconductivity tuned by field-controlled magnetization: URhGe, UCoGe, and UTe_2. *Phys. Rev. B* **104**, 014514 (2021).
38. Nevidomskyy, A. H. Stability of a nonunitary triplet pairing on the border of magnetism in UTe_2. Preprint at https://arxiv.org/abs/2001.02699 (2020).
39. Ishizuka, J., Sumita, S., Daido, A. & Yanase, Y. Insulator–metal transition and topological superconductivity in UTe_2 from a first-principles calculation. *Phys. Rev. Lett.* **123**, 217001 (2019).
40. Hazra, T. & Volkov, P. Pair-Kondo effect: a mechanism for time-reversal broken superconductivity and finite-momentum pairing in UTe_2. Preprint at https://arxiv.org/abs/2210.16293 (2022).
41. Chang, Y.-Y. et al. Topological Kondo superconductors. Preprint at https://arxiv.org/abs/2301.00538 (2023).

Methods

Sample growth and preparation

Single crystals of UTe_2 were grown by the chemical vapour transport method as described in refs. 7,42. Samples with one T_c (two T_c's) were grown in a two-zone tube furnace with temperatures of 950 °C and 860 °C (1,060 °C and 1,000 °C) at the hot and cold end, respectively.

Specimens were aligned to better than 1° using their magnetic anisotropy (performed in a Quantum Design MPMS) and X-ray diffraction (performed in a Laue backscattering system) measurements. Samples were then polished to produce two parallel faces normal to the (100), (010) and (001) directions, depending on the mode geometry (Extended Data Table 1).

Thin-film ZnO piezoelectric transducers were sputtered from a ZnO target in an atmosphere of oxygen and argon. Both shear and longitudinal responses are present in each transducer—the shear axis was aligned with either (100), (010) or (001), again depending on the particular mode geometry. Three crystals were measured in total (see Extended Data Table 1 for details). The shear response in our deposited transducers was achieved by mounting the sample on the far end of the sputtering sample stage, maximizing the distance between the sample and the ZnO target. The position of the sample stage was fixed during the entire deposition process (that is, rotation was disabled on the sample stage). The resulting polarization direction of the generated sound wave is then parallel to the shortest line drawn between the sample and the target—this orientation was verified using the absolute speed of sound and the moduli obtained using resonant ultrasound spectroscopy[43].

Pulse-echo ultrasound measurements

Measurements were performed in an Oxford Instruments Heliox ^{3}He refrigerator. We used a traditional phase-comparison pulse-echo ultrasound method to measure the change in elastic moduli relative to the highest temperature T_0; that is, we measured $\Delta c/c \equiv (c(T) - c(T_0))/c(T_0)$ Short bursts (typically ~50 ns) of radiofrequency signals, with the carrier frequency between 500 MHz and 2.5 GHz, were generated with a Tektronix TSG 4106A RF generator modulated by a Tektronix AFG 31052 arbitrary function generator, amplified by a Mini-Circuits ZHL-42W+ power amplifier, and transmitted to the transducer. The signal was detected with the same transducer, amplified with a Mini-Circuits ZX60-3018G-S+ amplifier and recorded on a Tektronix MSO64 oscilloscope. The detection amplifier was isolated from the power amplifier using Mini-Circuits ZFSWA2-63DR+ switches, timed with the same Tektronix AFG 31052 arbitrary function generator.

Both shear and compressional sound are generated by our transducers—these signals are separated in the time domain owing to the different speeds of propagation and identified as shear or compression using the known elastic moduli of UTe_2 (ref. 43). Extended Data Fig. 1 shows a raw pulse-echo signal from a transducer sputtered on sample S3 with sound propagating along the [010] direction with a shear polarization axis along [100], thus measuring c_{22} and c_{66} simultaneously. Echoes corresponding to the different elastic modes can be clearly identified as shear (vertical dashed red lines) and compression (vertical dashed blue lines).

The phase of each echo was analysed using a software lock-in, and the relative change in phase between two echoes was converted to the relative change in speed of sound as a function of temperature. In Extended Data Fig. 2, we compare the temperature dependence of c_{33} of samples S1 and S3 obtained with different transducers.

Data availability

Data that support the plots within this paper and other findings of this study are available via GitHub at https://github.com/CHiLL-Ramshaw/manuscripts-supporting_data/tree/0292ab9b15b60af93341e64b759507e4e59eb7cd/2024_Single_Component_Superconductivity_in_UTe2_at_Ambient_Pressure (ref. 44) and from the corresponding author upon reasonable request. Source data are provided with this paper.

References

42. Ran, S. et al. Comparison of two different synthesis methods of single crystals of superconducting uranium ditelluride. *J. Vis. Exp.* https://doi.org/10.3791/62563 (2021).
43. Theuss, F. et al. Resonant ultrasound spectroscopy for irregularly shaped samples and its application to uranium ditelluride. *Phys. Rev. Lett.* **132**, 066003 (2024).
44. Theuss, et al. 2024_single_component_superconductivity_in_UTe_2_at_ambient_pressure. *GitHub* https://github.com/CHiLL-Ramshaw/manuscripts-supporting_data/tree/0292ab9b15b60af93341e64b759507e4e59eb7cd/2024_Single_Component_Superconductivity_in_UTe2_at_Ambient_Pressure (2024).

Acknowledgements

We acknowledge helpful discussions with D. Agterberg and P. Brydon. We thank the Cornell LASSP Professional Machine Shop for their contributions to designing and fabricating equipment used in this study. A. Shragai, B.J.R. and F.T. acknowledge funding from the Office of Basic Energy Sciences of the United States Department of Energy under award number DE-SC0020143 (ultrasound experiments and analysis). N.P.B. and J.P. acknowledge support from the Department of Energy award number DE-SC-0019154 (sample characterization), the Gordon and Betty Moore Foundation's EPiQS Initiative through grant number GBMF9071 (materials synthesis), the National Science Foundation under grant number DMR-2105191 (sample preparation) and the Maryland Quantum Materials Center and the National Institute of Standards and Technology. B.J.R. and F.T. acknowledge use of the Cornell Center for Materials Research Shared Facilities which are supported through the NSF MRSEC programme (DMR-1719875). G.G. acknowledges support from the ANR grants STeP2 no ANR-22-EXES-0013 and QuantEx no ANR-23-CE30-0001-01.

Author contributions

B.J.R. conceived the experiment. I.M.H., S.R.S., Y.S.E. and A. Suarez grew and characterized the samples. F.T. and A. Shragai performed the sample preparation and transducer fabrication. F.T., A. Shragai and G.G. performed the ultrasound measurements. F.T. and B.J.R. performed the data analysis and mean-field calculations. T.S. performed density functional theory calculations. F.T. and B.J.R. wrote the paper with input from all other co-authors. J.P., N.P.B. and B.J.R. supervised the project.

Competing interests

The authors declare no competing interests.

Additional information

Extended data is available for this paper at https://doi.org/10.1038/s41567-024-02493-1.

Supplementary information The online version contains supplementary material available at https://doi.org/10.1038/s41567-024-02493-1.

Correspondence and requests for materials should be addressed to B. J. Ramshaw.

Peer review information *Nature Physics* thanks Tatsuya Yanagisawa and the other, anonymous, reviewer(s) for their contribution to the peer review of this work.

https://doi.org/10.1038/s41567-024-02493-1

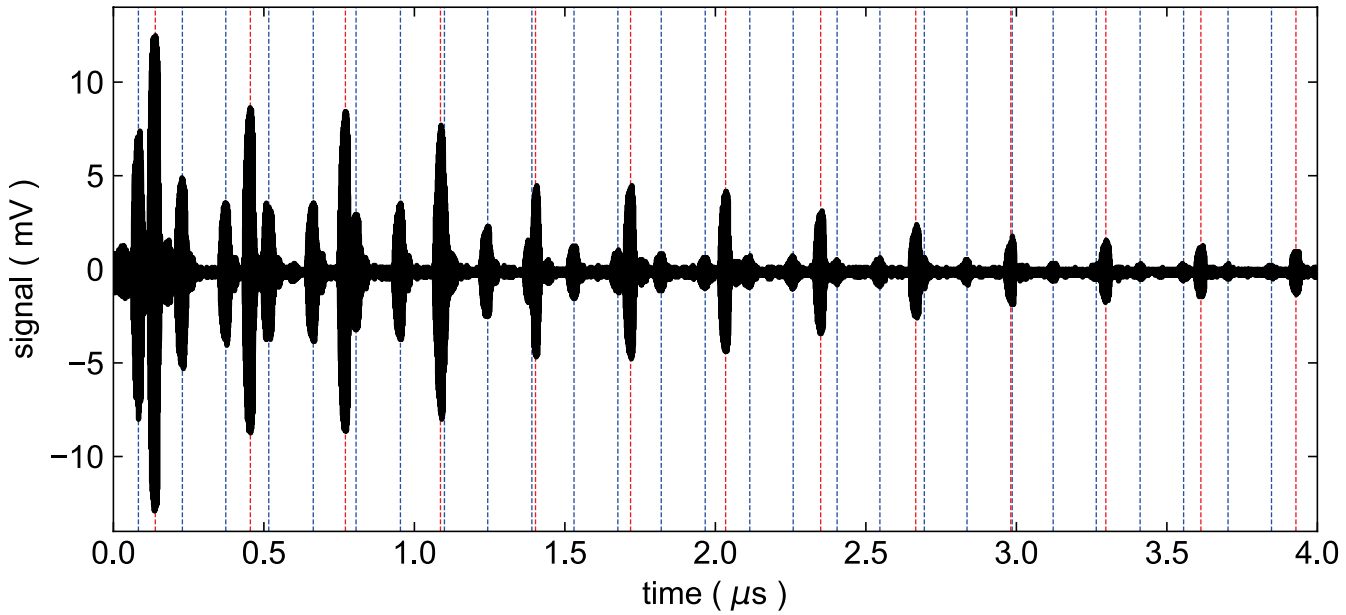

Extended Data Fig. 1 | Raw Pulse-Echo Signal. The raw signal from a sputtered ZnO shear transducer on sample S3 with sound propagation along the [010] and polarization along the [100] directions. The transducer exhibits both a compressional (blue lines) and a shear (red dashed lines) response. These correspond to sound modes determined by the elastic moduli c_{22} and c_{66}, respectively.

https://doi.org/10.1038/s41567-024-02493-1

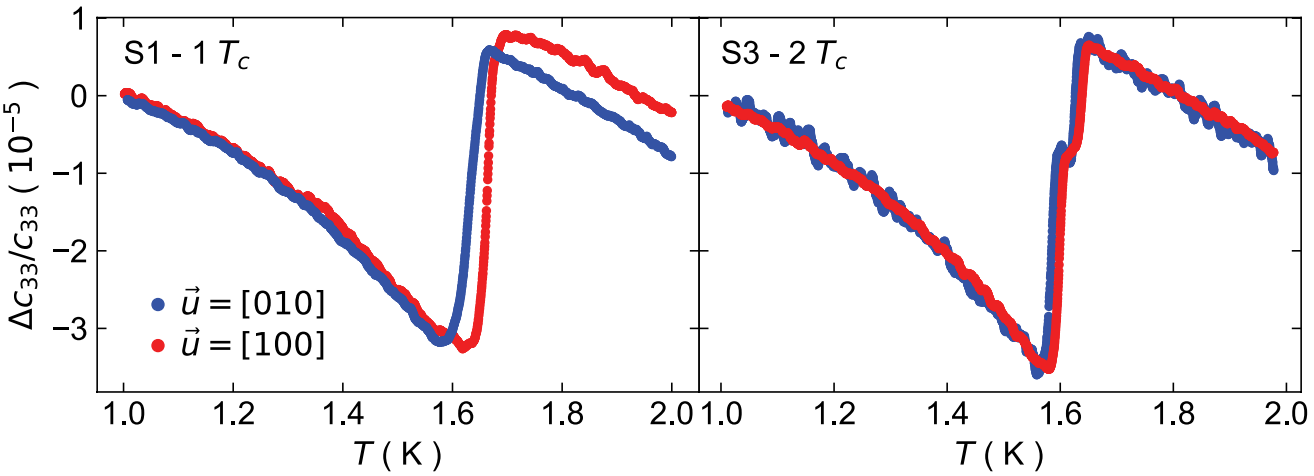

Extended Data Fig. 2 | Comparison of different transducers. Shown are $\Delta c_{33}/c_{33}$ for single T_c (S1, left) and two T_c (S3, right) samples. For each sample we compare the relative change in elastic modulus between measurements obtained with two different transducers. Both transducers excited sound along the [001] direction. However, for the data in red, the shear component of the transducer was polarized along [100] (additionally measuring c_{55}), whereas for the data in blue, the shear component of the transducer was polarized along [010] (additionally measuring c_{44}).

https://doi.org/10.1038/s41567-024-02493-1

Extended Data Table 1 | Pulse-echo ultrasound sample configurations

# T_c	Sample	$\vec{k}$	$\vec{u}$	c_{ij}	f (MHz)	d (μm)	c (GPa)
1	S1	[001]	[100]	c_{55}	1261	330 ± 17	51 ± 5
			[010]	c_{44}	1434	330 ± 17	27 ± 3
			[001]	c_{33}	2260	330 ± 17	91 ± 11
	S2	[100]	[100]	c_{11}	823	920 ± 46	81 ± 8
			[010]	c_{66}	1250	920 ± 46	28 ± 3
2	S3	[001]	[100]	c_{55}	1348	550 ± 28	52 ± 5
			[010]	c_{44}	1352	550 ± 28	28 ± 3
			[001]	c_{33}	1348	550 ± 28	88 ± 9
		[010]	[100]	c_{66}	1362	290 ± 15	30 ± 3
			[010]	c_{22}	1362	290 ± 15	141 ± 15

Listed are the transducer configurations for all the measurements in this manuscript. Samples are sorted by the number of superconducting phase transitions (first column). Additional information given is the propagation $\vec{k}$ and the polarization $\vec{u}$ of the sound pulse excited in the sample, as well as the measured elastic modulus. Also shown is the frequency at which each measurement is performed. We also provide the thicknesses d of the measured samples and the resulting absolute values of the elastic moduli obtained from the separation of echoes at room temperature. Uncertainties represent a 5% uncertainty in the thickness.

nature physics

Article

https://doi.org/10.1038/s41567-024-02493-1

Single-component superconductivity in UTe_2 at ambient pressure

In the format provided by the authors and unedited

CONTENTS

DATA REPRODUCIBILITY

Figure 1 and Figure 2 show the relative change of elastic moduli as a function of temperature as obtained when different echoes from a single experiment are used for the data analysis. Figure 3 and Figure 4 show the relative change of elastic moduli for different carrier frequencies of the excited sound pulse. We find no significant dependence on either the echoes, or the frequencies used for any of our measurements.

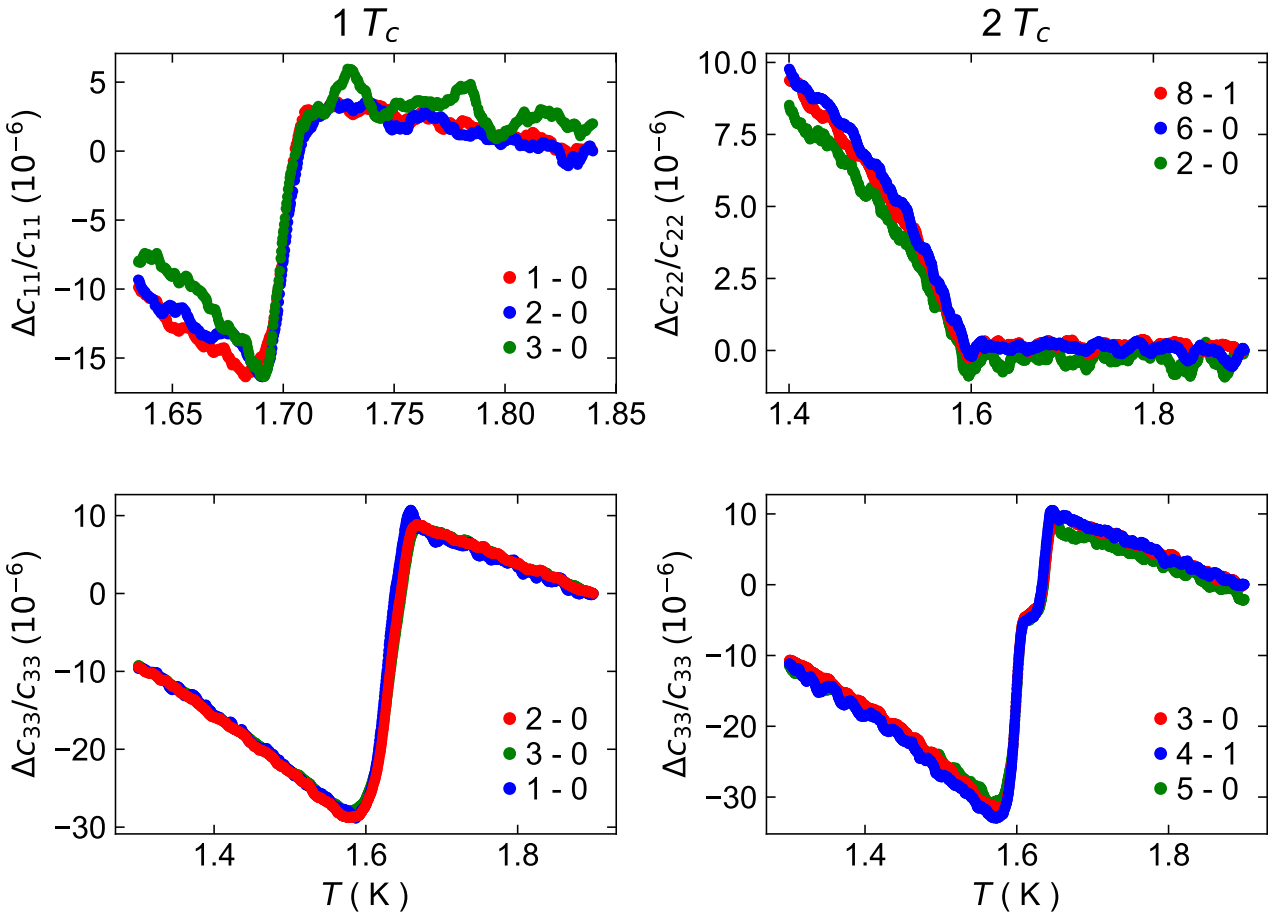

FIG. 1. **Echo Analysis Compressional Moduli.** The relative change of compressional elastic moduli as obtained from different echoes in a single pulse-echo ultrasound experiment. The colors indicate the echoes used for each curve. The data in red are the data shown in the main. The left column shows data for samples with one superconducting transition, the right column is for samples with two transitions.

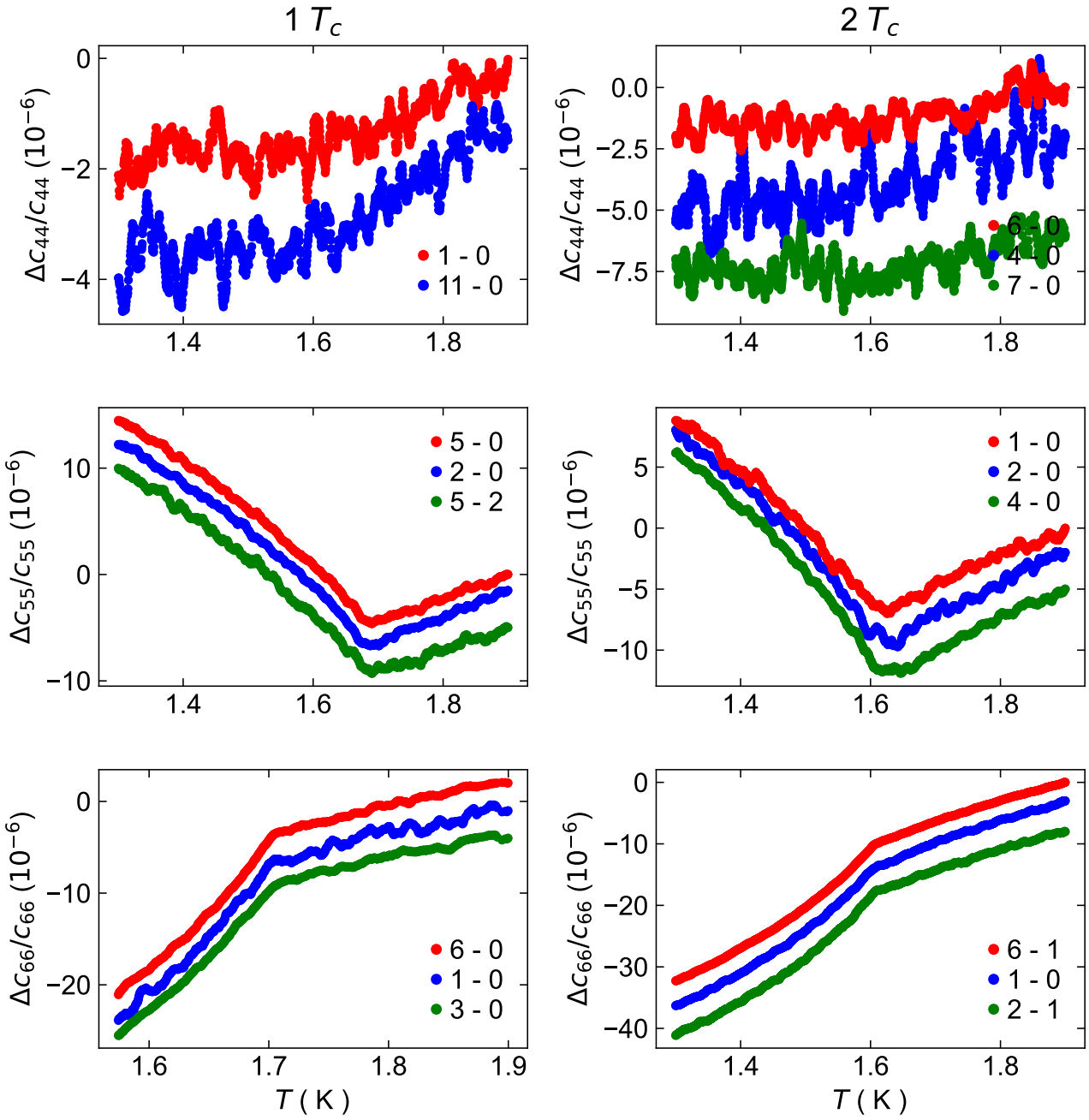

FIG. 2. **Echo Analysis Shear Moduli.** The relative change of shear elastic moduli as obtained from different echoes in a single pulse-echo ultrasound experiment. The colors indicate the echoes used for each curve. The data in red are the data shown in the main. The left column shows data for samples with one superconducting transition, the right column is for samples with two transitions.

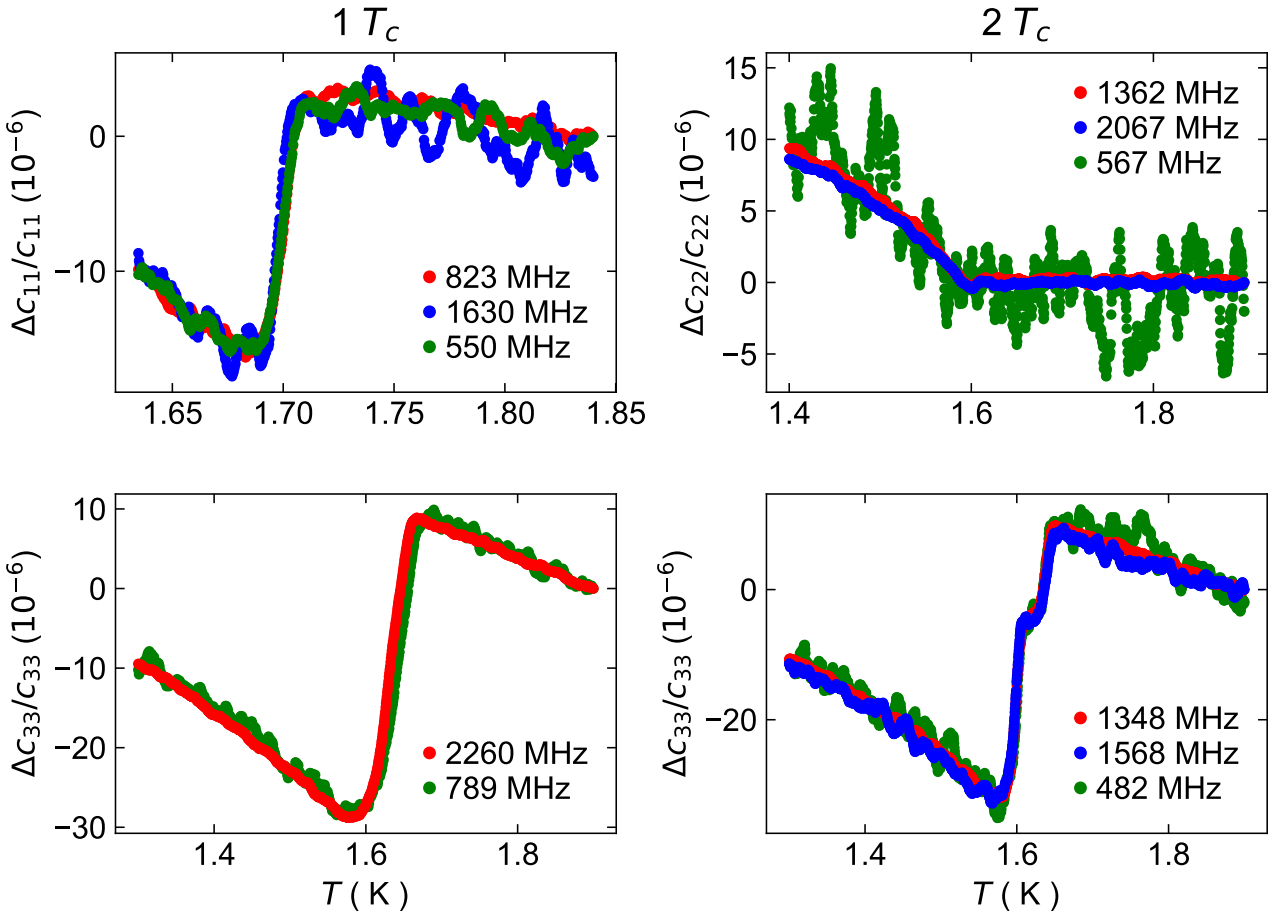

FIG. 3. **Frequency Dependence Compressional Moduli.** The relative change of compressional elastic moduli at different frequencies. The data in red are the data shown in the main. The left column shows data for samples with one superconducting transition, the right column is for samples with two transitions.

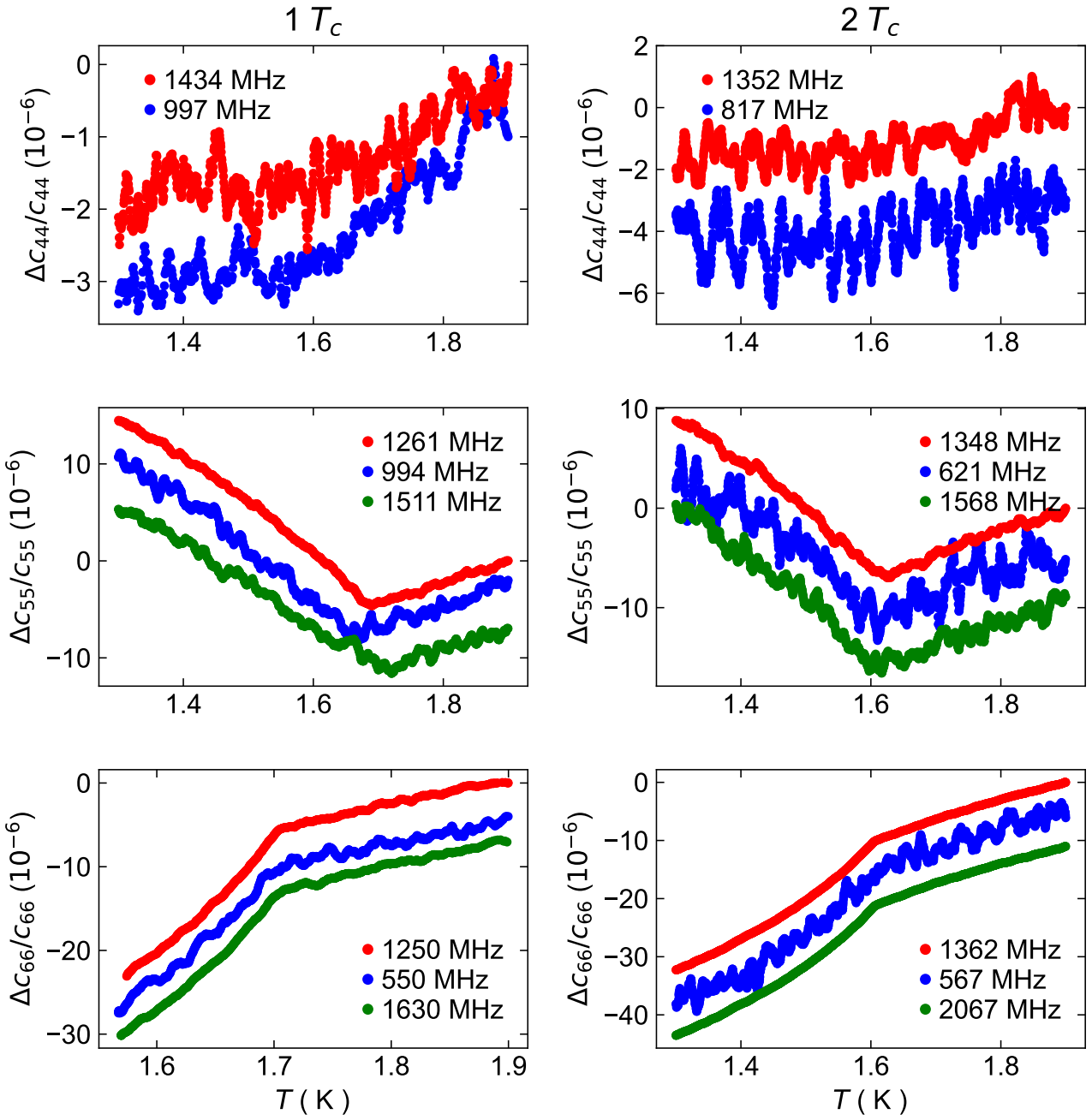

FIG. 4. **Frequency Dependence Shear Moduli.** The relative change of shear elastic moduli at different frequencies. The data in red are the data shown in the main. The left column shows data for samples with one superconducting transition, the right column is for samples with two transitions.

NOISE ANALYSIS

Figure 5 shows the relative change of all elastic moduli also shown in the main. In order to estimate the noise of our data, a second order polynomial has been fitted to the normal state data (highlighted by a red background in Figure 5). In Figure 6 we show the same elastic moduli with that polynomial subtracted from the data. We then estimate its noise as the RMS of the background-subtracted data above the transition, i.e. the same temperature range which we used to fit said polynomial background (red shaded region). The resulting RMS values lie between 0.04 ppm and 0.41 ppm (on average less than 1.9×10^{-7}).

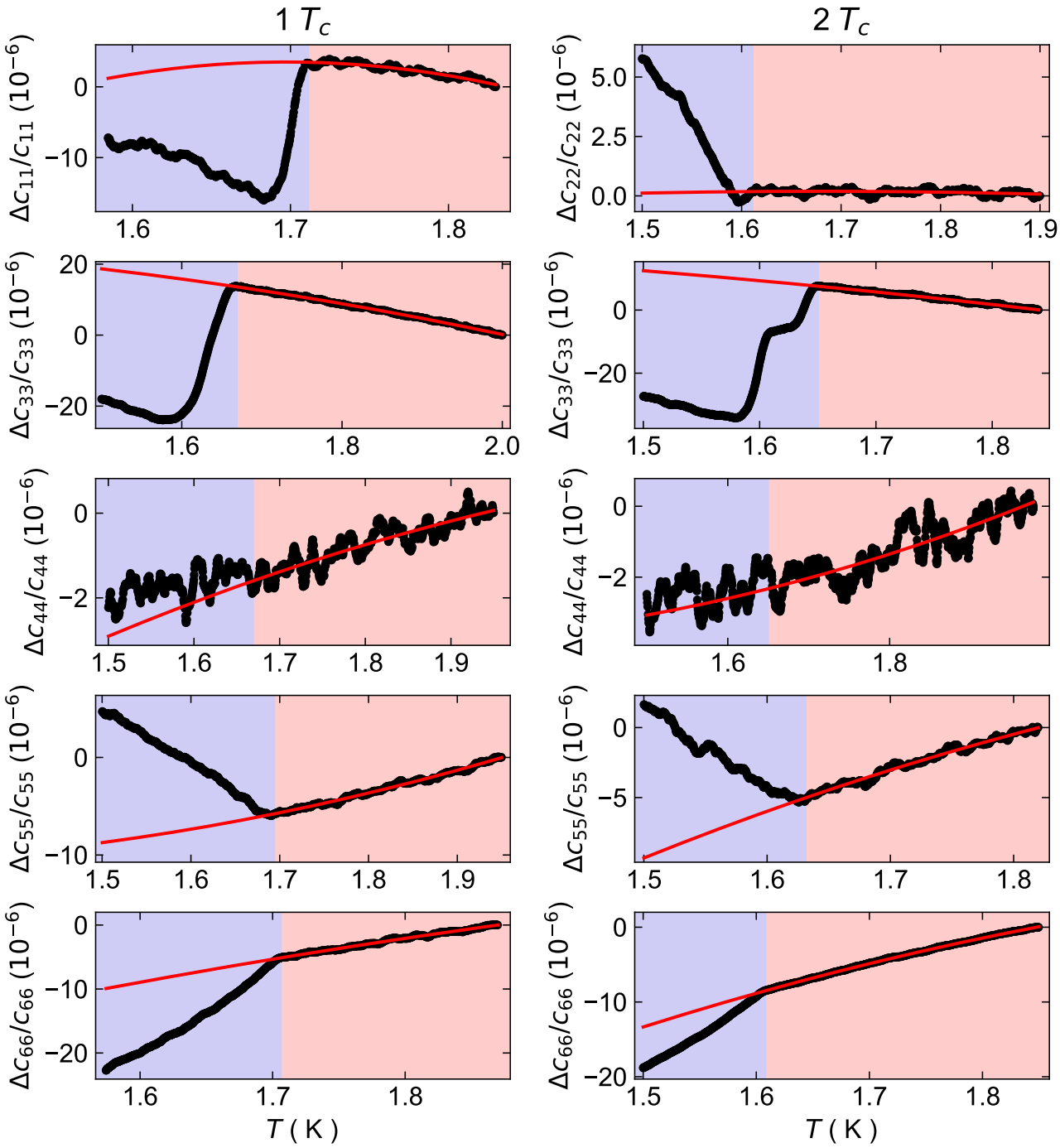

FIG. 5. **Background Subtraction.** Temperature dependence of all elastic moduli shown in the main (black points). A second order polynomial (red line) has been fitted to each modulus in the normal state above T_c (red shaded region). The left column shows data for samples with one superconducting transition, the right column is for samples with two transitions.

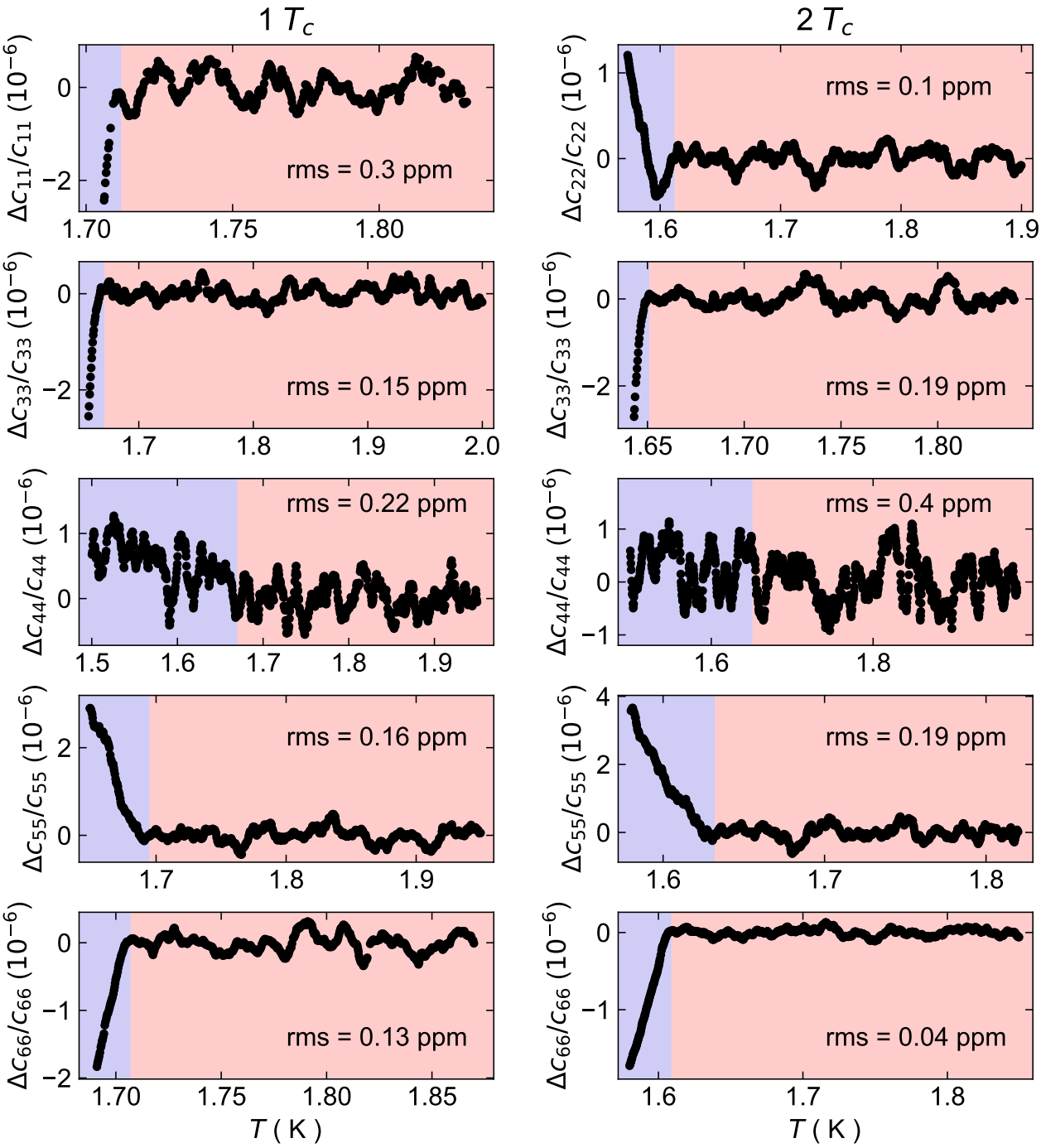

FIG. 6. **Noise Estimate.** Elastic moduli from Figure 5 with the normal state background (see Figure 5) subtracted. A RMS is calculated for each modulus in the same temperature range that was used to fit the background in Figure 5 (red shaded region). The purple/red shaded temperature regions are identical to those in Figure 5. The left column shows data for samples with one superconducting transition, the right column is for samples with two transitions.

LANDAU FREE ENERGY CALCULATIONS

Elastic moduli are the second derivative of the free energy with respect to strain, i.e. they are the strain susceptibility, in analogy with the heat capacity, which is the second derivative of the free energy with respect to temperature. If strain couples linearly to the square of the order parameter η (just like temperature does in the term $(T-T_c)\eta^2$), the respective elastic modulus will exhibit a discontinuity at the phase transition (just like the specific heat does). The reason for these discontinuities is that immediately below T_c, the system has a new degree of freedom that can respond when you apply strain (in the case of elastic moduli) or change temperature (in the case of heat capacity). This new degree of freedom means that the response below T_c is entirely distinct from that above T_c: even though the order parameter itself changes continuously, the system's susceptibility to changes in the order parameter is discontinuous.

For a single-component order parameter, only compressional moduli can exhibit this discontinuity. For a two-component order parameter, on the other hand, discontinuities in compressional moduli *and* certain shear moduli are allowed. This is because for single-component order parameters, the only quantity that can respond to strain is the magnitude of the order parameter. The bare "amplitude" of the order parameter breaks gauge symmetry and thus cannot enter directly into the free energy or couple linearly to external parameters like strain. As the magnitude of the order parameter is a scalar (simply a number), this means that it couples to scalar strains, i.e. compressional moduli.

For a two component order parameter, there are two new gauge-invariant quantities that can couple to strain: the relative phase between the components of the order parameter, and the overall "orientation" of the two components in order-parameter space. These are new degrees of freedom that can be probed by shear strain, and thus are what allow for discontinuities in the shear moduli at T_c.

Below, we elaborate on these concepts within the Landau theory of second-order phase transitions.

Elastic Free Energy

The elastic free energy of a solid is given by $\frac{1}{2}\sum_{i,j}\varepsilon_i c_{ij}\varepsilon_j$, with strain $\vec{\varepsilon}=\{\varepsilon_{xx},\varepsilon_{yy},\varepsilon_{zz},2\varepsilon_{yz},2\varepsilon_{xz},2\varepsilon_{xy}\}$ and the elastic tensor $\boldsymbol{c}$ in Voigt notation. In an orthorhombic crystal environment (i.e. point group D_{2h}), all individual elements of the strain tensor transform as a particular irreducible representation of the point group D_{2h}. In particular, we can rewrite

$$\vec{\varepsilon}=\{\varepsilon_{xx},\varepsilon_{yy},\varepsilon_{zz},2\varepsilon_{yz},2\varepsilon_{xz},2\varepsilon_{xy}\}=\{\varepsilon_{Ag,1},\varepsilon_{Ag,2},\varepsilon_{Ag,3},\varepsilon_{B3g},\varepsilon_{B2g},\varepsilon_{B1g}\}, \tag{1}$$

where the subscript now refers to the irreducible representation. Consequently, the elastic free energy can be rewritten as

$$\begin{aligned} f_{el}=&\frac{1}{2}\left(c_{Ag,1}\varepsilon_{Ag,1}^2+c_{Ag,2}\varepsilon_{Ag,2}^2+c_{Ag,3}\varepsilon_{Ag,3}^2+2c_{Ag,4}\varepsilon_{Ag,1}\varepsilon_{Ag,2}+2c_{Ag,5}\varepsilon_{Ag,1}\varepsilon_{Ag,3}+2c_{Ag,6}\varepsilon_{Ag,2}\varepsilon_{Ag,3}\right. \\ &\left.+c_{B3g}\varepsilon_{B3g}^2+c_{B2g}\varepsilon_{B2g}^2+c_{B2g}\varepsilon_{B2g}^2\right). \end{aligned} \tag{2}$$

Here, we have rewritten the elastic tensor according to

$$\boldsymbol{c}=\begin{pmatrix} c_{11} & c_{12} & c_{13} & 0 & 0 & 0 \\ c_{12} & c_{22} & c_{23} & 0 & 0 & 0 \\ c_{13} & c_{23} & c_{33} & 0 & 0 & 0 \\ 0 & 0 & 0 & c_{44} & 0 & 0 \\ 0 & 0 & 0 & 0 & c_{55} & 0 \\ 0 & 0 & 0 & 0 & 0 & c_{66} \end{pmatrix}=\begin{pmatrix} c_{Ag,1} & c_{Ag,4} & c_{Ag,5} & 0 & 0 & 0 \\ c_{Ag,4} & c_{Ag,2} & c_{Ag,6} & 0 & 0 & 0 \\ c_{Ag,5} & c_{Ag,6} & c_{Ag,3} & 0 & 0 & 0 \\ 0 & 0 & 0 & c_{B3g} & 0 & 0 \\ 0 & 0 & 0 & 0 & c_{B2g} & 0 \\ 0 & 0 & 0 & 0 & 0 & c_{B1g} \end{pmatrix}. \tag{3}$$

Order Parameter Free Energy and Coupling to Strain: One-Component Order Parameter

A single-component superconducting order parameter (OP) can be parametrized as $\eta e^{i\gamma}$, with an amplitude η and phase γ, both real. However, since the free energy needs to obey global gauge symmetry, the OP can only appear in even powers and the phase factor $e^{i\gamma}$ becomes unobservable. Only one degree of freedom remains, the amplitude (or superfluid density) η. The phase factor is thus dropped in the following discussion. In this case, the OP free energy expansion to fourth order reads

$$f_{OP}=\frac{a}{2}\eta^2+\frac{b}{4}\eta^4, \tag{4}$$

	One-Component OP $\eta_0 = \sqrt{\frac{-a}{b}}$	$B_{2u} + iB_{3u}$ $(\theta_0, \gamma_0) = (\pi/4, \pm\pi/2)$ $\eta_0 = \pm\sqrt{\frac{-2a_1}{b_1+b_3-b_4}}$
$\delta c_{A_g,i}$	$-\frac{g_i^2}{2b}\,(\eta)$	$\frac{a_1(-2a_2(b_1+b_3-b_4)g_i^a g_i^s + a_1(-(b_1+b_3-b_4)(g_i^a)^2 + 4b_2 g_i^a g_i^s - (b_1-b_3+b_4)(g_i^s)^2))}{a_1^2(b_1^2-4b_2^2-(b_3-b_4)^2)+4a_1a_2b_2(b_1+b_3-b_4)-a_2^2(b_1+b_3-b_4)^2}\,(\eta,\theta)$
δc_{B1g}	0	$-\frac{g_4^2}{2b_4}\,(\gamma)$
δc_{B2g}	0	0
δc_{B3g}	0	0

TABLE I. **Discontinuities in elastic moduli for different OP configurations.** Magnitudes of discontinuities in elastic moduli at T_c for one and two-component OPs, along with the particular degree of freedom that causes the discontinuity (given in parentheses after the expression for the discontinuity). For a one-component OP, only compressional moduli $c_{A_g,i}$ show a discontinuity, caused by fluctuations in the order parameter amplitude η. For a $B_{2u} + iB_{3u}$ two-component OP, compressional moduli and the c_{B1g} elastic modulus are allowed to show a discontinuity. The discontinuity in the compressional moduli is due to fluctuations in the absolute amplitdue η of the OP, as well as fluctuations in the relative amplitude θ between individual components. The discontinuity in c_{B1g}, however, is caused by fluctuations of the relative phase γ between different order parameter components.

where $a = a_0\,(T - T_c)$. $a_0 > 0$, and b are phenomenological constants, T_c is the critical temperature.

Since the OP has to appear in even powers in the free energy, the lowest possible coupling to strain is quadratic in OP and linear in strain. Furthermore, since the OP transforms as a one-dimensional irreducible representation of D_{2h}, its bilinear will always transform as the A_g irreducible representation, irrespective of the particular representation. Thus, quadratic in OP and linear in strain coupling terms are only allowed for A_g strains, and to lowest order, the terms in the free energy coupling the OP to strain are

$$f_{coupling} = \frac{1}{2}\left(g_1\varepsilon_{Ag,1} + g_2\varepsilon_{Ag,2} + g_3\varepsilon_{Ag,3}\right)\eta^2. \tag{5}$$

Following the formalism outlined in [1], coupling of strain to the OP leads to a discontinuity of the respective elastic moduli at T_c according to

$$\delta c_{mn} = -\frac{Z_m Z_n}{Y}\bigg|_{\eta\to\eta_0,\varepsilon_m\to 0}, \tag{6}$$

where $Z_m = \frac{\partial^2 f_{coupling}}{\partial\eta\partial\varepsilon_m}$, $Y = \frac{\partial^2 f_{OP}}{\partial\eta^2}$, and $\eta_0 = \sqrt{\frac{-a}{b}}$ is the equilibrium value for the OP defined by $\partial f_{OP}/\partial\eta = 0$. From Equation 6 it is straightforward to see that coupling terms in the free energy which are quadratic or higher order in strain will not lead to a discontinuity of the respective elastic modulus at T_c, which justifies the truncation of Equation 5 after terms linear in strain. Consequently, in the case of a one-component OP, no shear modulus (i.e. c_{B1g}, c_{B2g}, or c_{B3g}) is allowed to show a discontinuity at T_c (note that a discontinuity in its derivative is allowed [2]). This is a general statement purely based on the dimensionality of the order parameter and irrespective of its particular irreducible representation. Combining Equation 5 and Equation 6, all A_g elastic moduli exhibit a discontinuity at the critical temperature. The magnitudes of these discontinuities based on the free energy in Equation 4 and Equation 5 are summarized in Table I.

Order Parameter Free Energy and Coupling to Strain: Two-Component Order Parameter

Next we discuss discontinuities in the elastic moduli with a two-component OP $\boldsymbol{\eta} = \{\eta_x, \eta_y\}$. In the D_{2h} point group, all irreducible representations are one dimensional. A two-component order parameter therefore has to consist of two one-component order parameters, meaning η_x and η_y can belong to different irreducible representations and are not related by symmetry. The example of η_x and η_y transforming as the B_{2u} and B_{3u} irreducible representations, respectively, as suggested for the superconducting OP in UTe_2 by authors in Hayes *et al.* [3] and Wei *et al.* [4], will be used in the discussion below. For this particular OP, three independent bilinear combinations can be formed: $|\eta_x|^2$,

$|\eta_y|^2$, and $\left(\eta_x\eta_y^* + \eta_x^*\eta_y\right)$ transforming as A_g, A_g, and B_{1g} representations respectively. The Landau free energy reads

$$\begin{aligned} f_{OP} = &\frac{a_1}{2}\left(|\eta_x|^2 + |\eta_y|^2\right) + \frac{a_2}{2}\left(|\eta_x|^2 - |\eta_y|^2\right) \\ &+ \frac{b_1}{4}\left(|\eta_x|^4 + |\eta_y|^4\right) + \frac{b_2}{4}\left(|\eta_x|^4 - |\eta_y|^4\right) + \frac{b_3}{2}|\eta_x|^2|\eta_y|^2 + \frac{b_4}{4}\left(\left(\eta_x\eta_y^*\right)^2 + \left(\eta_x^*\eta_y\right)^2\right), \end{aligned} \tag{7}$$

where $a_{1,2} = a_{1,2}^{(0)}(T - T_c)$, $a_{1,2} > 0$, and b_i are phenomenological constants. Based on these considerations, the free energy coupling the OP to linear powers of strain can be written as

$$\begin{aligned} f_{coupling} = &\frac{1}{2}\left(g_1^s\varepsilon_{Ag,1} + g_2^s\varepsilon_{Ag,2} + g_3^s\varepsilon_{Ag,3}\right)\left(|\eta_x|^2 + |\eta_y|^2\right) + \frac{1}{2}\left(g_1^a\varepsilon_{Ag,1} + g_2^a\varepsilon_{Ag,2} + g_3^a\varepsilon_{Ag,3}\right)]\left(|\eta_x|^2 - |\eta_y|^2\right) \\ &+ \frac{g_4}{2}\varepsilon_{B1g}\left(\eta_x\eta_y^* + \eta_x^*\eta_y\right). \end{aligned} \tag{8}$$

Coupling of B_{1g} strain to the second power of the OP as in the free energy above is only possible for the particular example of a $\{B_{2u}, B_{3u}\}$ OP. However, linear coupling of shear strain (i.e. B_{1g}, B_{2g}, or B_{3g} strain in D_{2h}) to a bilinear of the OP is in general only possible for a two-component OP.

In order to calculate the discontinuities of elastic moduli in the presence of a two-component OP, Ghosh *et al.* [1] generalized the expression in Equation 6 to

$$\delta c_{mn} = -\boldsymbol{Z}_m^T\boldsymbol{Y}^{-1}\boldsymbol{Z}_n\Big|_{\boldsymbol{\eta}\to\boldsymbol{\eta}_0,\varepsilon_m\to 0}, \tag{9}$$

where $\boldsymbol{Z}_m = \frac{\partial^2 f_{coupling}}{\partial\boldsymbol{\eta}\partial\varepsilon_m}$ and $\boldsymbol{Y} = \frac{\partial^2 f_{OP}}{\partial\boldsymbol{\eta}^2}$. Parametrizing the OP as $\boldsymbol{\eta} = \eta\left\{\cos\theta, e^{i\gamma}\sin\theta\right\}$, the derivative $\partial/\partial\boldsymbol{\eta}$ becomes $\partial/\partial\left\{\eta,\theta,\gamma\right\}$. Assuming a chiral order parameter $(\theta_0,\gamma_0) = (\pi/4, \pm\pi/2)$, the equilibrium amplitude η_0, defined by $\partial f_{OP}/\partial\eta|_{\eta_0,\theta_0,\gamma_0} = 0$, is then given by $\eta_0 = \pm\sqrt{\frac{-2a_1}{b_1+b_3-b_4}}$. This assumption is motivated by the observation of time-reversal symmetry breaking (TRSB) [3, 4] in the superconducting state of UTe_2. For this order parameter configuration, one finds

$$\boldsymbol{Y} = \begin{pmatrix} a_1 + \frac{3\eta_0^2}{2}\left(b_1 + b_3 - b_4\right) & -2\eta_0\left(a_2 + b_2\eta_0^2\right) & 0 \\ -2\eta_0\left(a_2 + b_2\eta_0^2\right) & \left(b_1 - b_3 + b_4\right)\eta_0^4 & 0 \\ 0 & 0 & \frac{b_4\eta_0^4}{2} \end{pmatrix}, \tag{10}$$

$$\boldsymbol{Z}_{Ag,i} = \begin{pmatrix} g_i^s\eta_0 \\ -g_i^a\eta_0^2 \\ 0 \end{pmatrix}, \ \boldsymbol{Z}_{B1g} = \begin{pmatrix} 0 \\ 0 \\ -\frac{g_4\eta_0^2}{2} \end{pmatrix}, \ \boldsymbol{Z}_{B2(3)g} = \begin{pmatrix} 0 \\ 0 \\ 0 \end{pmatrix}, \tag{11}$$

where $i = 1, 2, 3$. From Equation 10 and Equation 11 in can be seen that for a chiral $\{B_{2u}, B_{3u}\}$ order parameter in a D_{2h} point group, all compressional moduli (i.e. the elastic moduli corresponding to A_g strains) show a step discontinuity at T_c due to coupling of the corresponding strain to the absolute amplitude of the OP (the superfluid density), as well as the relative amplitude of the different components (this is in contrast to a multi-component OP where the different components are related by symmetry, for which compressional strains only couple to the absolute amplitude of the OP [1]). Among all the shear moduli, only c_{B1g} shows a step discontinuity at T_c, due to the coupling of B_{1g} shear strain to the relative phase between the different components of the OP.

While the details of the above calculation depend on the exact OP parameter configuration, the main statement is general: a multi-component OP is required for a discontinuity in any shear modulus.

HEAT CAPACITY MEASUREMENTS

Heat capacity measurements (Figure 7) were performed in a ^{3}He cryostat using the quasi-adiabatic method: a fixed power was applied to the calorimeter to raise it approximately 1% over the bath temperature. The power was then turned off to allow the calorimeter to relax back to the bath temperature. The heat capacity was extracted from these heating and cooling data by fitting them to exponentially-saturating curves. The sample was affixed to the calorimeter with Apiezon N grease. The background heat capacity of the grease and the calorimeter were measured separately and subtracted from the data in Figure 7.

EHRENFEST ANALYSIS

The discontinuity observed in the compressional moduli δc_{ii} at T_c is directly related to the jump in the heat capacity divided by temperature, $\Delta C/T$, via Ehrenfest relations. For a single component order parameter they read

$$\delta c_{ii} = -\frac{\Delta C}{T}\left(\frac{dT_c}{d\varepsilon_{ii}}\right)^2. \tag{12}$$

The derivative of critical temperature with respect to compressional strain $dT_c/d\varepsilon_{ii}$ can therefore be calculated by extracting the discontinuities of the corresponding elastic modulus and the heat capacity at T_c. The heat capacity was measured in sample S3 (see Figure 7) and the size of its discontinuity at T_c is determined to be (196 ± 18) mJ/(mol K^2). The magnitudes of the discontinuities in $\Delta c/c$ for all compressional moduli are extracted according to Figure 8 and the values are given in Table II. Using these values, as well as the elastic moduli of UTe_2 [5], the absolute values of $dT_c/d\varepsilon_{ii}$ ($ii = xx, yy, zz$) are calculated (see Table II).

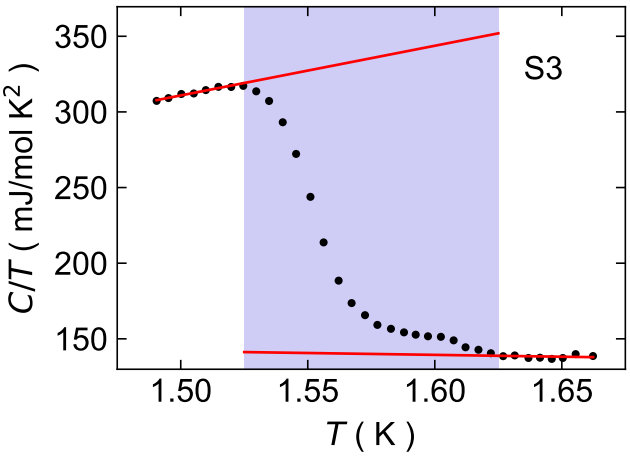

FIG. 7. **Heat Capacity.** Heat capacity divided by temperature as a function of temperature measured on sample S3. The jump at T_c is (196 ± 18) mJ/(mol K^2), determined according to linear fits below and above the transition (red lines). The uncertainty is estimated from the finite temperature range close to T_c in which the data deviates significantly from these fits. This range is indicated by the blue shaded region.

The derivatives of the critical temperature with respect to stress can be calculated from the derivatives with respect to strain via

$$\begin{pmatrix} dT_c/d\sigma_{xx} \\ dT_c/d\sigma_{yy} \\ dT_c/d\sigma_{zz} \end{pmatrix} = \begin{pmatrix} c11 & c12 & c13 \\ c12 & c22 & c23 \\ c13 & c23 & c33 \end{pmatrix}^{-1} \begin{pmatrix} dT_c/d\varepsilon_{xx} \\ dT_c/d\varepsilon_{yy} \\ dT_c/d\varepsilon_{zz} \end{pmatrix}. \tag{13}$$

The resulting values are given in Table II, along with values measured in uniaxial stress experiments [6]. The elastic tensor used for this calculation is again taken from Theuss *et al.* [5]. Note that the analysis in Equation 13 requires knowledge about the signs of $dT_c/d\varepsilon_{ii}$, whereas the Ehrenfest relations in Equation 12 only yield their absolute values. For a correct analysis from our data, signs according to Girod *et al.* [6] were assumed.

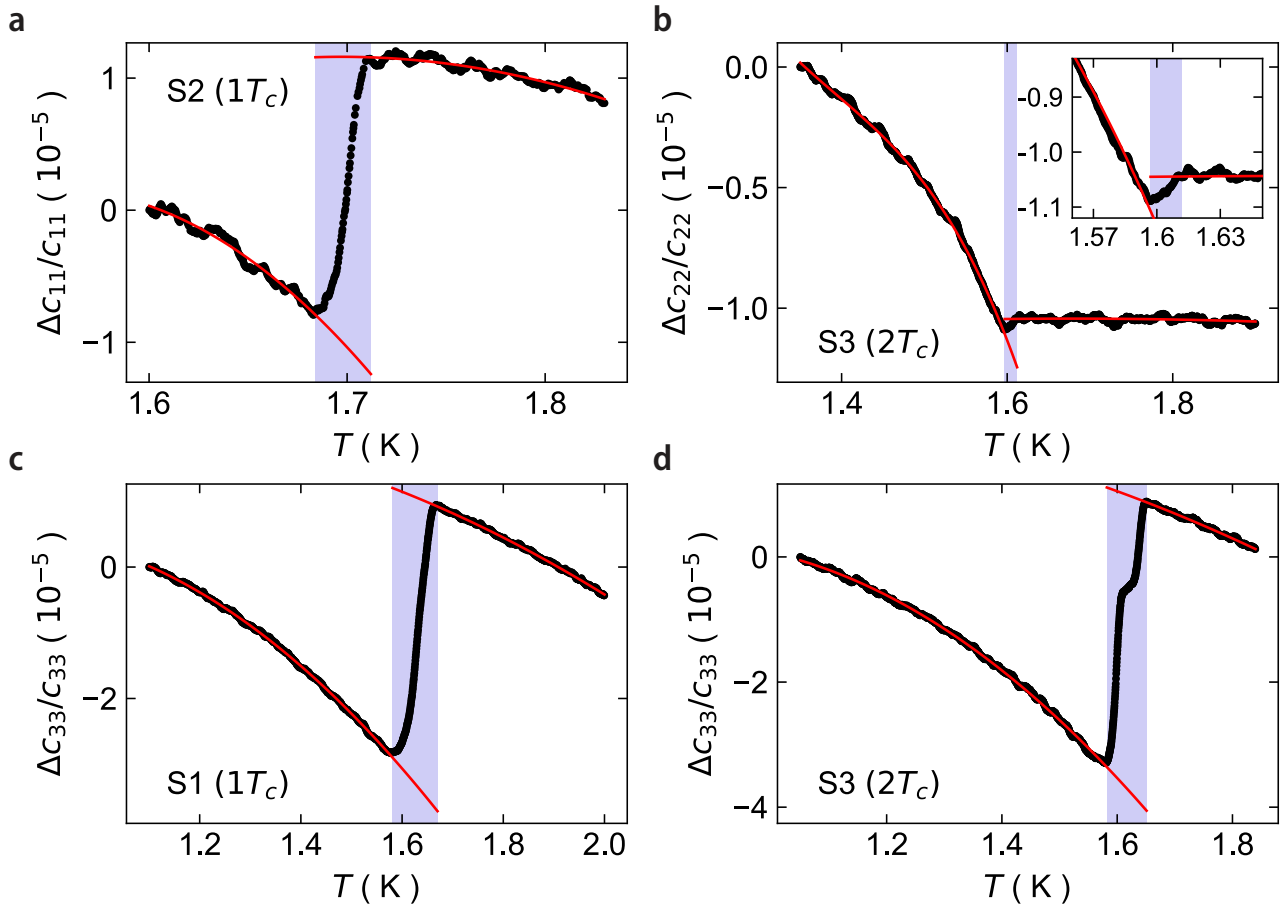

FIG. 8. **Step Discontinuities in Compressional Moduli.** Relative changes in compressional moduli across T_c (black points). The magnitude of the step discontinuity in compressional moduli is defined as the difference between polynomial fits to the data above and below T_c (red lines). The uncertainty is estimated from the finite temperature range close to T_c in which the data deviates significantly from these fits (indicated in blue). Extracted values are given in Table II. The elastic moduli shown are c_{11} (panel a) and c_{33} (panel c) for samples with one transition and c_{22} (panel b) and c_{33} (panel d) for samples with two transitions. The inset of panel b shows the relative change in c_{22} close to T_c.

Elastic Modulus	Step in $\frac{\Delta c}{c}$	$\frac{dT_c}{d\varepsilon_{ii}}$ $\left(\frac{\mathrm{K}}{\%\,\mathrm{strain}}\right)$	$\frac{dT_c}{d\sigma_{ii}}$ $\left(\frac{\mathrm{K}}{\mathrm{GPa}}\right)$	$\frac{dT_c}{d\sigma_{ii}}$ $\left(\frac{\mathrm{K}}{\mathrm{GPa}}\right)$ from [6]
c_{11} $(1T_c)$	$-(2.2 \pm 0.2) \times 10^{-5}$	-0.23 ± 0.02	-0.50 ± 0.03	-0.87
c_{22} $(2T_c)$	$-(0.13 \pm 0.07) \times 10^{-5}$	-0.07 ± 0.02	-0.09 ± 0.02	—
c_{33} $(1T_c)$	$-(4.4 \pm 0.3) \times 10^{-5}$	0.34 ± 0.02	0.60 ± 0.03	0.56
c_{33} $(2T_c)$	$-(4.7 \pm 0.2) \times 10^{-5}$	0.35 ± 0.02	0.62 ± 0.03	0.56

TABLE II. **Ehrenfest Analysis.** Derivatives of the critical temperature with respect to strain $dT_c/d\varepsilon$ are calculated based on the magnitudes of the discontinuities in $\Delta c/c$ extracted according to Figure 8. Values of the absolute elastic moduli and respective uncertainties are taken from Theuss *et al.* [5] and the size of the specific heat jump (or more precisely $\Delta C/T$) is taken to be 196 ± 18 mJ/(mol K^2) from Figure 7. Knowledge of the signs of $dT_c/d\varepsilon$ is required for the correct calculation of $dT_c/d\sigma$. Since 12 only yields their absolute value, the signs are chosen according to uniaxial stress experiments [6]. The last column shows a comparison to values from said uniaxial stress experiments in Girod *et al.* [6].

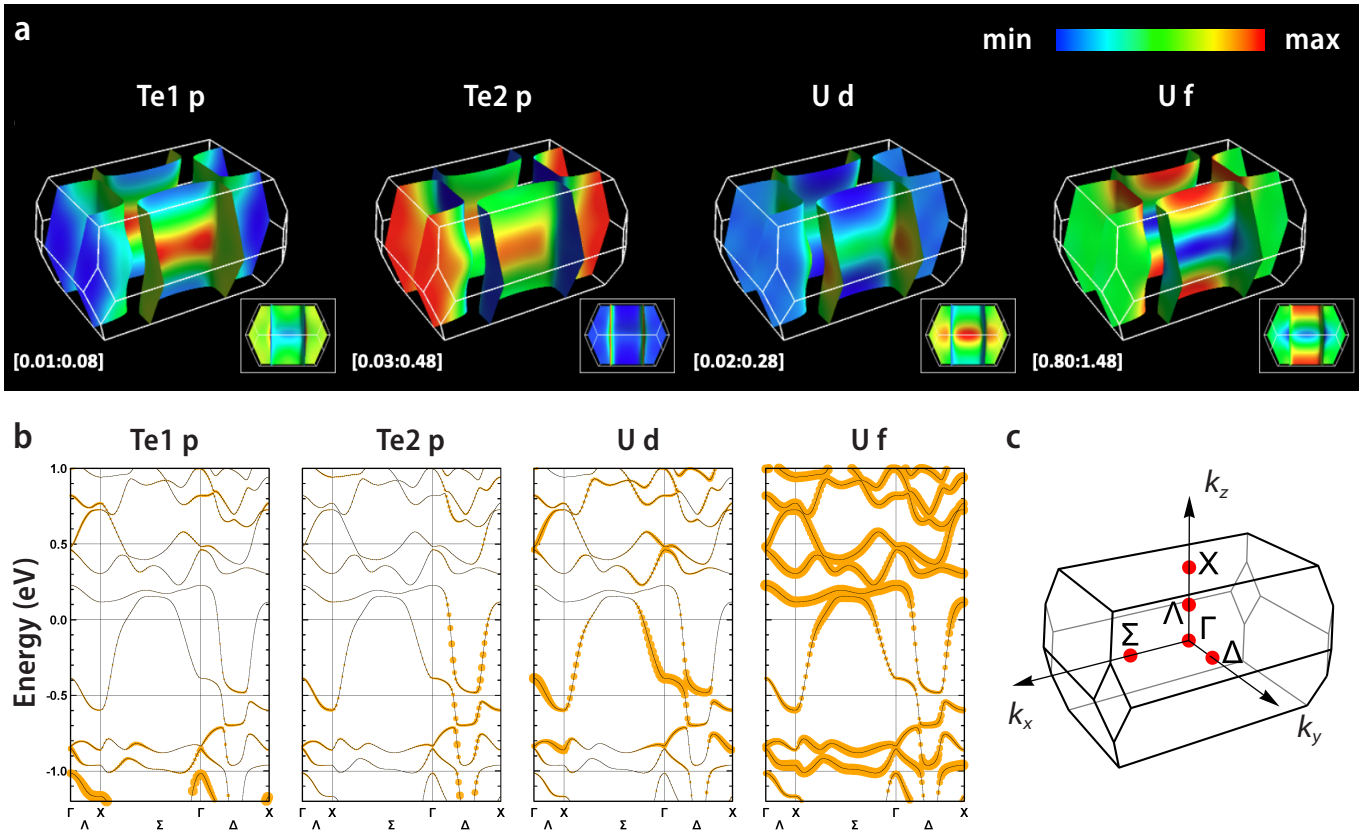

FIG. 9. **DFT Fermi Surface and Band Structure.** (a) Fermi surface of UTe_2 calculated with $U = 2$ eV. Fermi surfaces are colored according to their orbital Te1 p, Te2 p, U d, and U f content, from left to right, respectively. Color scales are rescaled between each plot, but respective minimum and maximum values are given to the bottom left of each panel. (b) Band structure calculated with the same parameters as in (a). Orange circles are sized according to the orbital weight of Te1 p, Te2 p, U d, and U f (from left to right) on each individual band. (c) UTe_2 Brillouin zone.

UTE_2 FERMI SURFACE AND SUPERCONDUCTING GAP

Density Functional Theory

Density-functional theory calculations are used to examine the orbital character of the electronic states in the vicinity of the chemical potential. The self-consistent field calculation is performed in the same way as in Theuss *et al.* [5], by additionally considering the Hubbard U for the uranium $5f$ electrons. The full-potential linearized augmented plane wave method [7] calculations employed the generalized gradient approximation [8] for the exchange correlation, wave function and potential energy cutffs of 16 and 200 Ry, respectively, and muffin-tin sphere radii of 1.35 Å. Spin-orbit coupling was fully taken into account in the assumed nonmagnetic state. We set $U = 2$ eV to obtain a quasi 2D Fermi surface [9, 10], which qualitatively accounts for the recent experiments. Along the high-symmetry lines in the Brillouin zone (Λ, Σ, and Δ lines, see Figure 9c) and on a dense $50\times50\times50$ k-point mesh, the (Kramers degenerate) band energy and wave functions are generated, and the orbital components of each doublet are calculated within the atom-centered spheres of radius 1.35 Å. In Figure 9, the orbital components are shown on the Fermi surface (panel a—the visualization of the Fermi surface is done with `FermiSurfer` [11]) and along the band dispersion (panel b).

Tight Binding Model

Figure 9 motivates a tight binding model constructed from two quasi-one-dimensional chain Fermi surfaces: one chain from the Te(2) $5p$ orbitals, and one from the U $6d$ orbitals. This model faithfully captures the shape of the Fermi surface measured by quantum oscillations (see [12]). This Fermi surface is quite similar to that calculated for $ThTe_2$,

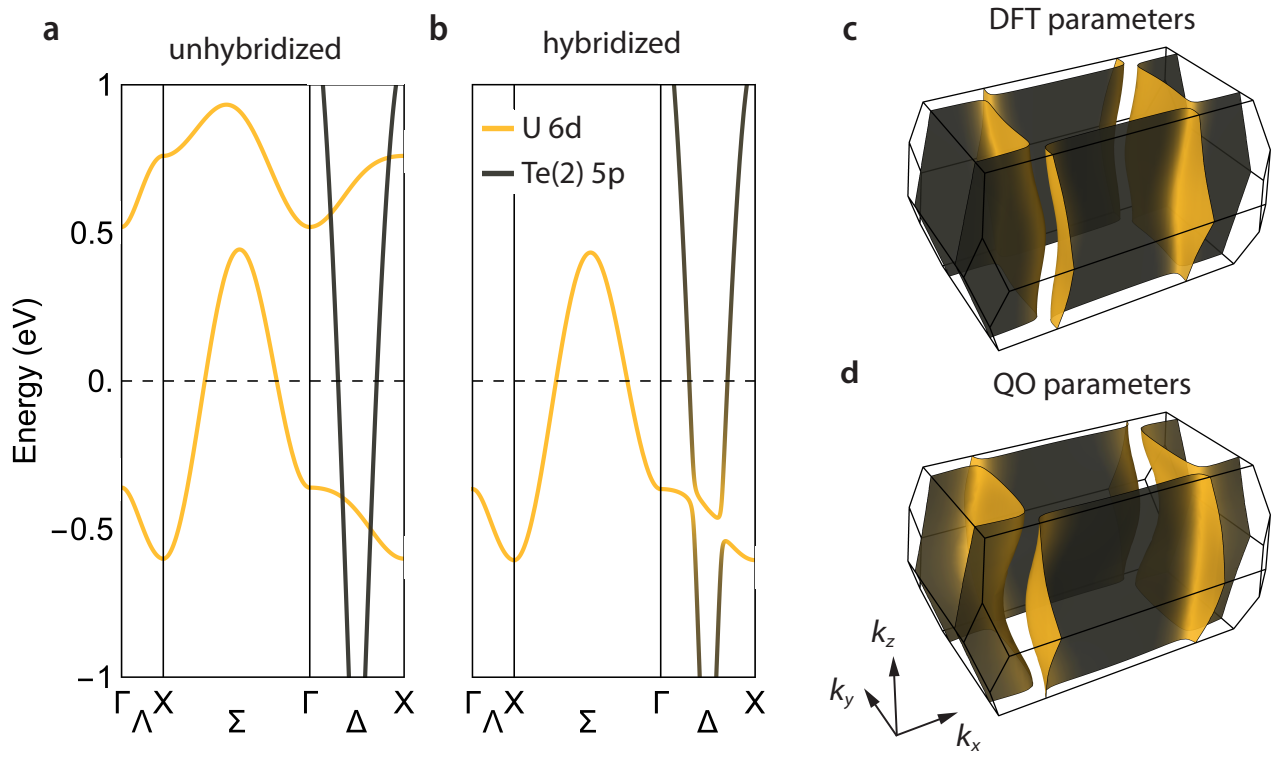

FIG. 10. **Tight Binding Model.** (a-c) Tight binding model with parameters to match DFT results. (a) Unhybridized bands formed by uranium 6*d* (yellow) and tellurium (2) 5*p* (gray) electrons. Bands crossing the Fermi level are hybridized in (b) and the resulting Fermi surface is shown in (c). Colors represent a projection on original U/Te(2) bands. (d) Fermi surface from tight binding model with parameters to match quantum oscillation results [12].

which has no f electrons—while the f electrons in UTe_2 hybridize strongly with both bands, the predominant effect is to enhance the cyclotron masses and shift the chemical potential, without strongly modifying the Fermi surface shape.

There are two uranium atoms that form a dimer in the center of the conventional unit cell shown in Figure 5a of the main text. The dominant tight binding parameters will be the chemical potential $\mu_{\rm U}$, the intra-dimer overlap $\Delta_{\rm U}$, the hopping $t_{\rm U}$ along the uranium chain in the a direction, the hopping $t'_{\rm U}$ to other uranium in the dimer along the chain direction, the hoppings $t_{ch,{\rm U}}$ and $t'_{ch,{\rm U}}$ between chains in the $a-b$ plane, and the hopping $t_{z,{\rm U}}$ between chains along the c axis. The two bands from the two uranium sites then come from diagonalizing the following matrix:

$$E_{\rm U} = \begin{bmatrix} \mu_{\rm U} - 2t_{\rm U}\cos k_x a - 2t_{ch,{\rm U}}\cos k_y b & -\Delta_{\rm U} - 2t'_{\rm U}\cos k_x a - 2t'_{ch,{\rm U}}\cos k_y b - 4t_{z,{\rm U}}e^{-ik_z c/2}\cos k_x\frac{a}{2}\cos k_y\frac{b}{2} \\ -\Delta_{\rm U} - 2t'_{\rm U}\cos k_x a - 2t'_{ch,{\rm U}}\cos k_y b - 4t_{z,{\rm U}}e^{ik_z c/2}\cos k_x\frac{a}{2}\cos k_y\frac{b}{2} & \mu_{\rm U} - 2t_{\rm U}\cos k_x a - 2t_{ch,{\rm U}}\cos k_y b \end{bmatrix}. \tag{14}$$

There are in principle 4 Te(2) sites per conventional unit cell, but by including only nearest-neighbor hopping in the $a-b$ plane, the problem is again reduced to diagonalizing a 2×2 matrix. The dominant tight binding parameters are then the chemical potential $\mu_{\rm Te}$, the intra-unit-cell overlap $\Delta_{\rm Te}$ between the two Te(2) atoms along the chain direction, the hopping $t_{\rm Te}$ along the Te(2) chain in the b direction, the hopping $t_{ch,{\rm Te}}$ between chains in the a direction, and the hopping $t_{z,{\rm Te}}$ between chains along the c axis. The tight binding matrix is:

$$E_{\rm Te} = \begin{bmatrix} \mu_{\rm Te} - 2t_{ch,{\rm Te}}\cos k_x a & -\Delta_{\rm Te} - t_{\rm te}e^{-ik_y b} - 2t_{z,{\rm Te}}\cos k_z\frac{c}{2}\cos k_x\frac{a}{2}\cos k_y\frac{b}{2} \\ -\Delta_{\rm Te} - t_{\rm te}e^{ik_y b} - 2t_{z,{\rm Te}}\cos k_z\frac{c}{2}\cos k_x\frac{a}{2}\cos k_y\frac{b}{2} & \mu_{\rm Te} - 2t_{ch,{\rm Te}}\cos k_x a \end{bmatrix}. \tag{15}$$

The resultant bands are plotted in Figure 10a. The tight binding parameters were chosen to roughly match the DFT result shown in Figure 9 and are given in Table III. The two bands crossing the Fermi energy can be hybridized to form the electron and hole pocket. We use an isotropic in momentum hybridization δ and chose its value to roughly match the DFT result. The resultant two bands that cross the Fermi energy are shown in Figure 10b, and the 3D Fermi surface is shown in Figure 10c. The predominant difference between the FS calculated with $U = 2$ eV and the FS reported by Eaton *et al.* [12] is that the latter was chosen with the opposite-sign dispersion along the c-axis. Tight binding parameters chosen to roughly match the FS reported in Eaton *et al.* [12] are also given in Table III, with the resultant FS shown in Figure 10d.

	Δ_{U}	t_{U}	t'_{U}	$t_{ch,\mathrm{U}}$	$t'_{ch,\mathrm{U}}$	$t_{z,\mathrm{U}}$	μ_{Te}	Δ_{Te}	t_{Te}	$t_{ch,\mathrm{Te}}$	$t_{z,\mathrm{Te}}$	δ
DFT	0.40	0.15	0.08	0.01	0.00	-0.03	-1.80	-1.50	-1.50	0.00	-0.05	0.09
QO	0.05	0.10	0.08	0.01	0.00	0.04	-1.80	-1.50	-1.50	-0.03	-0.5	0.10

TABLE III. All parameters given in eV.

Superconducting Gap

When considering the symmetries of superconducting gaps, it is necessary to distinguish the cases of weak and strong spin-orbit coupling: UTe_2 likely falls in the latter category. However, since the orthorhombic point group of UTe_2 (D_{2h}) is inversion symmetric, one can still label irreducible representations as even or odd. This classification is used to distinguish spin singlet (even) or triplet (odd) superconductors. Since UTe_2 is most likely a spin-triplet superconductor, the possible irreducible representations of the order parameter are A_u, B_{1u}, B_{2u}, and B_{3u}. In the strong spin-orbit limit, they correspond to the following $\vec{d}$-vectors [13]

$$\vec{d}_{A_u} = \{\alpha k_x, \beta k_y, \gamma k_z\}, \tag{16}$$

$$\vec{d}_{B_{1u}} = \{\alpha k_y, \beta k_x, \gamma k_x k_y k_z\}, \tag{17}$$

$$\vec{d}_{B_{2u}} = \{\alpha k_z, \beta k_x k_y k_z, \gamma k_x\}, \tag{18}$$

$$\vec{d}_{B_{3u}} = \{\alpha k_x k_y k_z, \beta k_z, \gamma k_y\}, \tag{19}$$

where α, β, and γ are real constants and the momentum dependence of the superconducting gap is given by

$$\Delta\left(\vec{k}\right) = \sqrt{\vec{d}\cdot\vec{d}^{\star} \pm \left|\vec{d}\times\vec{d}^{\star}\right|}. \tag{20}$$

Here, $\vec{d}^{\star}$ is the complex conjugate of $\vec{d}$. The A_u order parameter is fully gapped, whereas the B_{1u}, B_{2u}, and B_{3u} order parameters have point nodes along the k_z, k_y, and k_x directions respectively. A B_{1u} gap is thus also fully gapped on the Fermi surface of UTe_2 found by quantum oscillations [12, 14] and only exhibits point nodes on a putative Fermi pocket enclosing the Γ-point [15].

The gap structures shown in the main text are calculated at $k_z = 0$ with $\alpha = \beta = \gamma$. A slight anisotropy in these parameters can change the exact shape of the momentum dependence of the different gap symmetries, but will not change their nodal structure.

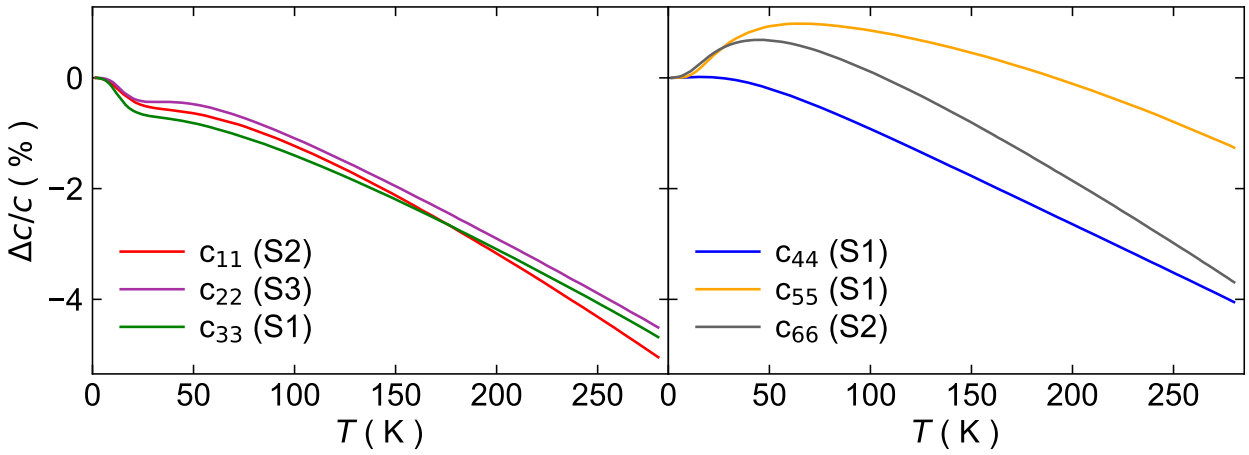

FIG. 11. **Normal State Elastic Moduli.** Relative changes of the normal state elastic moduli of UTe_2 from about 2 K to 280 K. Compressional moduli (c_{11}, c_{22}, c_{33}) and shear moduli (c_{44}, c_{55}, c_{66}) are shown in the left and right panels, respectively. The elastic moduli were measured at the following frequencies: 829 MHz (c_{11}), 1316 MHz (c_{22}), 1392 MHz (c_{33}), 1392 MHz (c_{44}), 1436 MHz (c_{55}), 829 MHz (c_{66}). Our measurements of c_{33}, c_{44}, and c_{55} agree with the data previously reported by Ushida *et al.* [16].

[1] S. Ghosh, A. Shekhter, F. Jerzembeck, N. Kikugawa, D. A. Sokolov, M. Brando, A. P. Mackenzie, C. W. Hicks, and B. J. Ramshaw, Thermodynamic evidence for a two-component superconducting order parameter in Sr_2RuO_4, Nature Physics **17**, 199 (2021).

[2] B. J. Ramshaw, A. Shekhter, R. D. McDonald, J. B. Betts, J. N. Mitchell, P. H. Tobash, C. H. Mielke, E. D. Bauer, and A. Migliori, Avoided valence transition in a plutonium superconductor, Proceedings of the National Academy of Sciences of the United States of America **112**, 3285 (2015).

[3] I. M. Hayes, D. S. Wei, T. Metz, J. Zhang, Y. S. Eo, S. Ran, S. R. Saha, J. Collini, N. P. Butch, D. F. Agterberg, A. Kapitulnik, and J. Paglione, Multicomponent superconducting order parameter in UTe_2, Science **373**, 797 (2021).

[4] D. S. Wei, D. Saykin, O. Y. Miller, S. Ran, S. R. Saha, D. F. Agterberg, J. Schmalian, N. P. Butch, J. Paglione, and A. Kapitulnik, Interplay between magnetism and superconductivity in UTe_2, Physical Review B **105**, 024521 (2022).

[5] F. Theuss, G. d. l. F. Simarro, A. Shragai, G. Grissonnanche, I. M. Hayes, S. Saha, T. Shishidou, T. Chen, S. Nakatsuji, S. Ran, M. Weinert, N. P. Butch, J. Paglione, and B. J. Ramshaw, Resonant ultrasound spectroscopy for irregularly shaped samples and its application to uranium ditelluride, Phys. Rev. Lett. **132**, 066003 (2024).

[6] C. Girod, C. R. Stevens, A. Huxley, E. D. Bauer, F. B. Santos, J. D. Thompson, R. M. Fernandes, J.-X. Zhu, F. Ronning, P. F. S. Rosa, and S. M. Thomas, Thermodynamic and electrical transport properties of UTe_2 under uniaxial stress, Physical Review B **106**, L121101 (2022).

[7] M. Weinert, G. Schneider, R. Podloucky, and J. Redinger, FLAPW: Applications and implementations, Journal of Physics: Condensed Matter **21**, 084201 (2009).

[8] J. P. Perdew, K. Burke, and M. Ernzerhof, Generalized Gradient Approximation Made Simple, Phys. Rev. Lett. **77**, 3865 (1996).

[9] J. Ishizuka, S. Sumita, A. Daido, and Y. Yanase, Insulator-metal transition and topological superconductivity in UTe_2 from a first-principles calculation, Physical Review Letters **123**, 217001 (2019).

[10] T. Shishidou, H. G. Suh, P. M. R. Brydon, M. Weinert, and D. F. Agterberg, Topological band and superconductivity in UTe_2, Physical Review B **103**, 104504 (2021).

[11] M. Kawamura, Fermisurfer: Fermi-surface viewer providing multiple representation schemes, Computer Physics Communications **239**, 197 (2019).

[12] A. G. Eaton, T. I. Weinberger, N. J. M. Popiel, Z. Wu, A. J. Hickey, A. Cabala, J. Pospíšil, J. Prokleška, T. Haidamak, G. Bastien, P. Opletal, H. Sakai, Y. Haga, R. Nowell, S. M. Benjamin, V. Sechovský, G. G. Lonzarich, F. M. Grosche, and M. Vališka, Quasi-2d fermi surface in the anomalous superconductor UTe_2, Nature Communications **15**, 223 (2024).

[13] J. F. Annett, Symmetry of the order parameter for high-temperature superconductivity, Advances in Physics **39**, 83 (1990).

[14] D. Aoki, H. Sakai, P. Opletal, Y. Tokiwa, J. Ishizuka, Y. Yanase, H. Harima, A. Nakamura, D. Li, Y. Homma, Y. Shimizu, G. Knebel, J. Flouquet, and Y. Haga, First observation of the de Haas–van Alphen Effect and Fermi surfaces in the unconventional superconductor UTe_2, Journal of the Physical Society of Japan **91**, 083704 (2022).

[15] L. Miao, S. Liu, Y. Xu, E. C. Kotta, C.-J. Kang, S. Ran, J. Paglione, G. Kotliar, N. P. Butch, J. D. Denlinger, and L. A. Wray, Low Energy Band Structure and Symmetries of UTe 2 from Angle-Resolved Photoemission Spectroscopy, Physical Review Letters **124**, 10.1103/PhysRevLett.124.076401 (2020).

[16] K. Ushida, T. Yanagisawa, R. Hibino, M. Matsuda, H. Hidaka, H. Amitsuka, G. Knebel, J. Flouquet, and D. Aoki, Lattice instability of UTe_2 studied by ultrasonic measurements, JPS Conference Proceedings **38**, 011021 (2023).